Cell Reports

Article

Coordinated ARP2/3 and glycolytic activities regulate the morphological and functional fitness of human CD8+ T cells

Graphical abstract

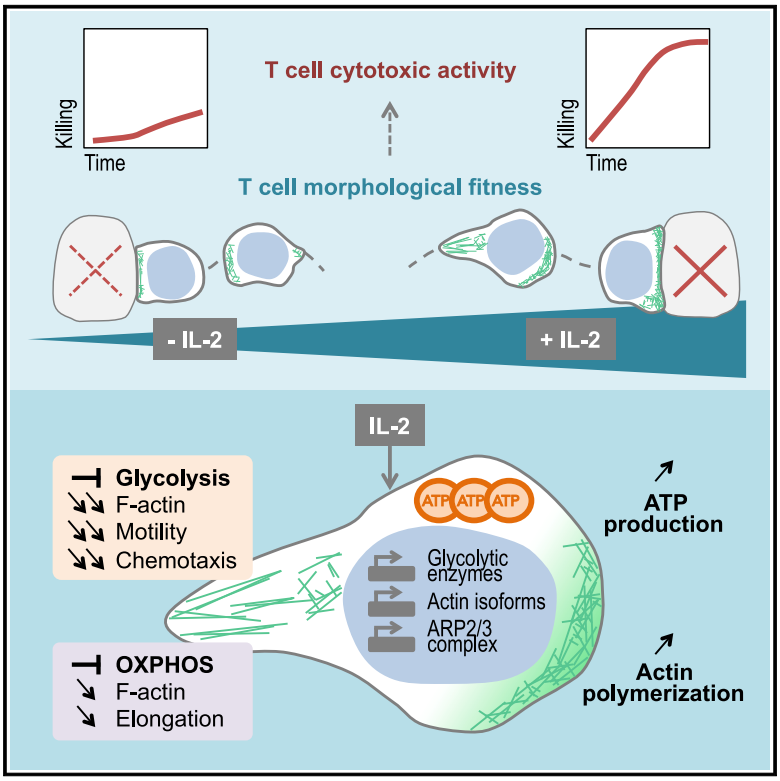

Highlights

- The morphological fitness of effector CD8+ T cells scales with their cytotoxic activity
- By promoting glycolysis, IL-2 boosts cell elongation and immunological synapse formation
- IL-2 upregulates glycolytic enzymes, actin, and ARP2/3 subunits in CD8+ T cells
- Glycolysis, rather than OXPHOS, sustains lamellipodial F-actin during CD8+ T cell function

Authors

Anton Kamnev, Tanvi Mehta, Matthias Wielscher, ..., Matthias Farlik, Kaan Boztug, Loïc Dupré

Correspondence

loic.dupre@meduniwien.ac.at

In brief

Effector cytotoxic T cells are known to depend on actin remodeling and glycolysis for their function. Kamnev et al. report the coordinated upregulation of actin, ARP2/3 subunits, and glycolytic enzymes upon IL-2 stimulation. ATP production, mainly via glycolysis, is required for lamellipodial F-actin polymerization during migration and synaptic adhesion.

Kamnev et al., 2024, Cell Reports *43*, 113853
March 26, 2024
https://doi.org/10.1016/j.celrep.2024.113853

CellPress

Cell Reports

CellPress
OPEN ACCESS

Article

Coordinated ARP2/3 and glycolytic activities regulate the morphological and functional fitness of human CD8$^+$ T cells

Anton Kamnev,[1,2,10] Tanvi Mehta,[1,2,10] Matthias Wielscher,[1] Beatriz Chaves,[3,4,5] Claire Lacouture,[3] Anna-Katharina Mautner,[1] Lisa E. Shaw,[1] Michael Caldera,[6] Jörg Menche,[6,7] Wolfgang P. Weninger,[1] Matthias Farlik,[1] Kaan Boztug,[2,6,8,9] and Loïc Dupré[1,2,3,11,*]

[1]Department of Dermatology, Medical University of Vienna, Vienna, Austria
[2]Ludwig Boltzmann Institute for Rare and Undiagnosed Diseases (LBI-RUD), Vienna, Austria
[3]Toulouse Institute for Infectious and Inflammatory Diseases (INFINITy), INSERM, CNRS, Toulouse III Paul Sabatier University, Toulouse, France
[4]National Institute of Science and Technology on Neuroimmunomodulation (INCT-NIM), Oswaldo Cruz Institute, Oswaldo Cruz Foundation (Fiocruz), Rio de Janeiro, Brazil
[5]Computational Modeling Group, Oswaldo Cruz Foundation (Fiocruz), Eusébio, Brazil
[6]CeMM Research Center for Molecular Medicine of the Austrian Academy of Sciences, Vienna, Austria
[7]Max Perutz Labs, University of Vienna, Vienna, Austria
[8]St. Anna Children's Cancer Research Institute (CCRI), Vienna, Austria
[9]Department of Pediatrics and Adolescent Medicine, Medical University of Vienna, Vienna, Austria
[10]These authors contributed equally
[11]Lead contact
*Correspondence: loic.dupre@meduniwien.ac.at
https://doi.org/10.1016/j.celrep.2024.113853

SUMMARY

Actin cytoskeleton remodeling sustains the ability of cytotoxic T cells to search for target cells and eliminate them. We here investigated the relationship between energetic status, actin remodeling, and functional fitness in human CD8$^+$ effector T cells. Cell spreading during migration or immunological synapse assembly mirrored cytotoxic activity. Morphological and functional fitness were boosted by interleukin-2 (IL-2), which also stimulated the transcription of glycolytic enzymes, actin isoforms, and actin-related protein (ARP)2/3 complex subunits. This molecular program scaled with F-actin content and cell spreading. Inhibiting glycolysis impaired F-actin remodeling at the lamellipodium, chemokine-driven motility, and adhesion, while mitochondrial oxidative phosphorylation blockade impacted cell elongation during confined migration. The severe morphological and functional defects of ARPC1B-deficient T cells were only partially corrected by IL-2, emphasizing ARP2/3-mediated actin polymerization as a crucial energy state integrator. The study therefore underscores the tight coordination between metabolic and actin remodeling programs to sustain the cytotoxic activity of CD8$^+$ T cells.

INTRODUCTION

The actin cytoskeleton is composed of dynamic networks of filaments that drive cell shape, polarity, migration, and the assembly of intercellular contacts.[1] The actin cytoskeleton is crucial for the function of immune cells due to their high motility and dynamic interaction with multiple partner cells. This applies to effector T cells, which are endowed with a high capacity to migrate to inflamed tissues and to establish immunological synapses (ISs) with target cells.[2,3] Morphological fitness of effector T cells, defined here as their propensity to remodel cell shape in response to motility and IS stimuli, is therefore expected to affect their efficiency at controlling infected cells and tumors.

The control of actin dynamics in T cells has so far mostly been viewed from the angle of the molecules composing the complex actin-remodeling machinery. In particular, the relevance of actin remodeling in immune cells, including T cells, has been highlighted by the discovery of approximately 20 inborn errors of immunity (IEIs) caused by deficiencies in actin binding proteins and their upstream regulators.[4] However, another key facet of actin-remodeling control relates to the high energetic cost of actin polymerization,[5] implying that ATP availability might set the magnitude of actin-remodeling-driven processes. The concept of coordination between ATP production and actin remodeling in T cells undergoing migration or IS assembly is supported by the observation of a polarized position of mitochondria at the uropod[6] and around the central domain of T cell receptors (TCRs) at the IS,[7] respectively. In response to interleukin-2 (IL-2) and during the acquisition of effector function, T cells switch from mitochondrion-dependent oxidative phosphorylation

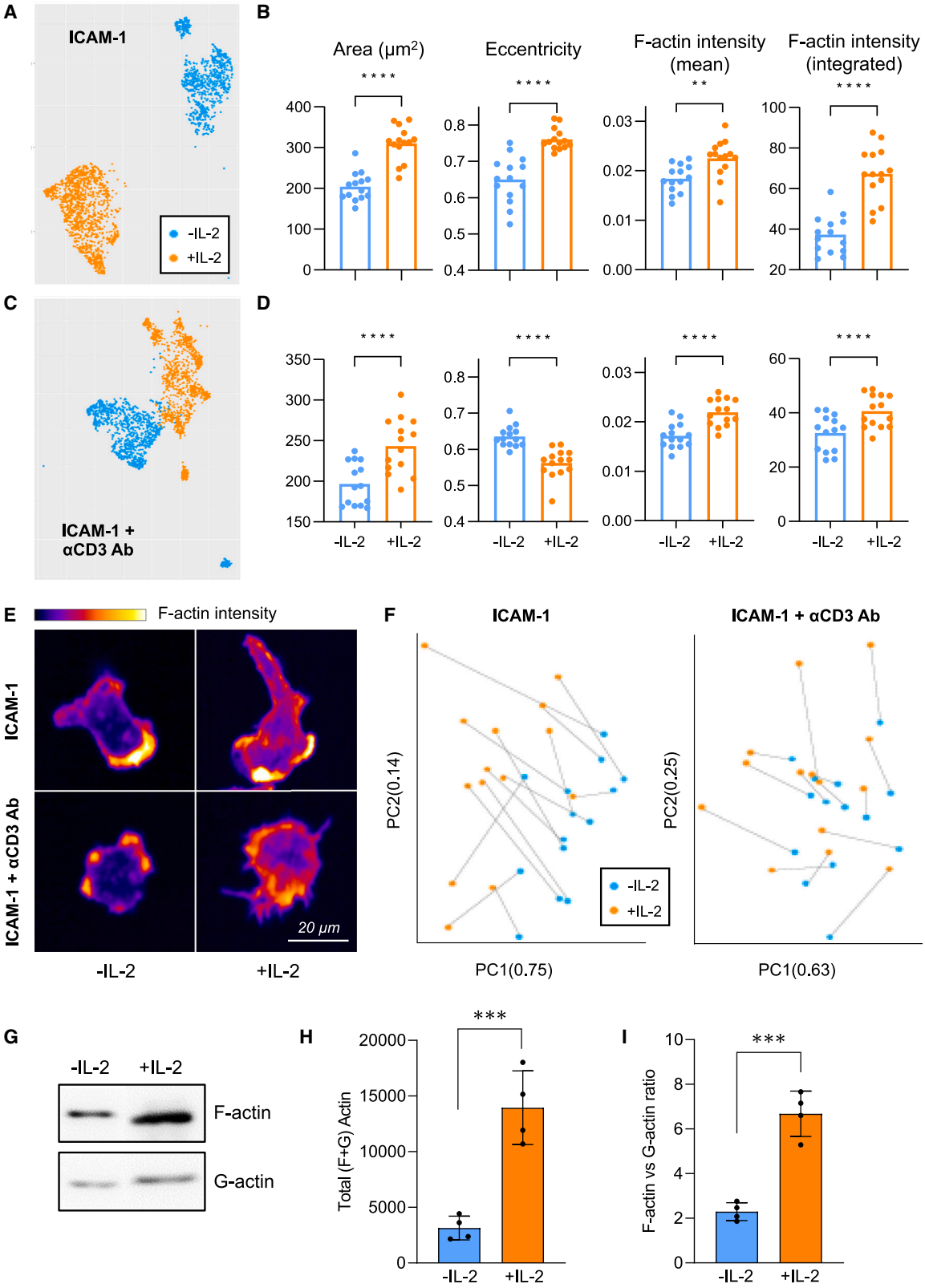

(legend on next page)

(OXPHOS) to aerobic glycolysis.[8–11] How such metabolic reprogramming might affect actin-remodeling activity and morphological fitness remains to be addressed.

We here set out to explore how the morphological properties of human effector CD8$^+$ T cells relate to their cytotoxic activity and how they might be influenced by their metabolic status. Our study uncovers that the ability of T cells to spread during migration and IS assembly is a crucial determinant of the cytotoxic activity. Our data further indicate that, during IL-2 stimulation, the morphological fitness of T cells scales with the transcriptional activation of glycolysis, actin isoforms, and ARP2/3 complex subunits, which is accompanied by a rise in ATP content and F/G-actin ratio. Blockade of glycolysis and examination of T cells from patients with deficiencies of Wiskott-Aldrich syndrome protein (WASP), hematopoietic Protein-1 (HEM1), and ARPC1B confirmed the pivotal roles of glycolysis and the ARP2/3 complex in controlling T cell fitness. Collectively, our data highlight that the metabolic status of cytotoxic CD8$^+$ T cells tunes their actin-remodeling machinery in the context of motility and synaptic adhesion.

RESULTS

IL-2 stimulates morphological fitness in effector CD8$^+$ T cells

To precisely characterize the propensity of IL-2 to stimulate the morphological response of human T cells, we established a collection of expanded effector CD8$^+$ T cells from 14 healthy donors to account for possible individual heterogeneity. We took advantage of a recently established high-content imaging (HCI) pipeline tailored to the morphological profiling of lymphocyte populations[12] to systematically extract and compare morphological features from IL-2-deprived vs. IL-2-exposed T cells. T cells were deposited on microwells pre-coated with either ICAM-1 or a combination of ICAM-1 and anti-CD3 antibodies (Abs) to stimulate a migratory behavior or IS assembly, respectively. Cells were then stained with DAPI and phalloidin-AF488 (Figures S1A and S1B). Overnight IL-2 exposure stimulated a T cell morphological response to ICAM-1 and ICAM-1/anti-CD3 Abs across all 14 samples, as shown by the clear segregation of IL-2-deprived and IL-2-treated cells on the Uniform Manifold Approximation and Projection (UMAP) schemes (Figures 1A and 1C). Independent from the coated stimulus and the IL-2 treatment, individual samples segregated on the UMAPs (Figures S2A and S2B), confirming that our HCI was able to capture donor-specific T cell morphological signatures.[12] Hallmarks of the IL-2-evoked morphological remodeling on both ICAM-1 and ICAM-1/anti-CD3 Abs were elevated spreading area and F-actin intensity, as detected at the interface with the stimulatory surface (Figures 1B and 1D). This possibly reflects an adjustment of F-actin content to a global increase in cell size.[13] IL-2 exposure led to an increase of eccentricity (ovalness of the ellipse fitting the cell contour, defined as the ratio of the distance from the center to the foci of the ellipse and the distance from the center to the vertices) over ICAM-1 and a decrease of the same parameter over ICAM-1/anti-CD3 Abs. Visual inspection of the cells spreading over ICAM-1 indicated that IL-2 exposure sustained the assembly of an F-actin-rich lamellipodial protrusion and cell elongation, explaining the increase of eccentricity (Figure 1E). Over ICAM-1/anti-CD3 Abs, IL-2 promoted radial spreading and peripheral F-actin enrichment, in line with the decrease of eccentricity. Principal-component analysis (PCA) with a restricted set of morphological parameters (Figure 1F) further indicated that, in the context of ICAM-1 challenge, IL-2 exposure boosted all selected features in a uniform manner, while mostly eccentricity explained variability among individual donors (Figure S2C and S2D). Although IL-2 robustly augmented the morphological response of each tested sample, it did not reduce the level of inter-individual heterogeneity comparable with that of the IL-2-deprived samples. In the context of ICAM-1/anti-CD3 Abs, the restricted set of parameters used in the PCA was not sufficient to discriminate the effects of IL-2 and inter-individual heterogeneity. To discriminate between the possibilities that IL-2 could impact global actin content or specifically stimulate actin polymerization, G-actin and F-actin contents were measured in IL-2-deprived vs. IL-2-exposed T cells (Figure 1G). IL-2 exposure resulted in a robust rise of total actin (Figure 1H). IL-2 also led to an increase of the F/G-actin ratio

Figure 1. IL-2 exposure stimulates the morphological fitness of effector CD8$^+$ T cells

(A) Morphological profiling of human CD8$^+$ T cells stimulated over ICAM-1, following exposure to IL-2, as indicated. UMAP plots correspond to the aggregation of 173 features extracted from automatically acquired confocal images. They highlight the distinct morphological profile of IL-2-treated cells on both stimuli. Each dot represents a pool of 20 individual cells. Data are derived from 14 healthy donors.

(B) Individual morphological features discriminating the IL-2 treatment condition were extracted and plotted. Each dot represents the average of CD8$^+$ T cells from each donor stimulated with ICAM-1. Eccentricity represents the elongation of the cells. The higher the eccentricity, the greater is the elongation of the cells.

(C) Morphological profiling of human CD8$^+$ T cells stimulated over ICAM-1/anti-CD3 Abs following exposure to IL-2, as indicated. UMAP plots correspond to the aggregation of 173 features extracted from automatically acquired confocal images. They highlight the distinct morphological profile of IL-2-treated cells on both stimuli. Each dot represents a pool of 20 individual cells. Data are derived from 14 healthy donors.

(D) Individual morphological features discriminating the IL-2 treatment condition were extracted and plotted. Each dot represents the average of CD8$^+$ T cells from each donor stimulated with ICAM-1/anti-CD3 Abs. Eccentricity represents the elongation of the cells. The higher the eccentricity, the greater is the elongation of the cells.

(E) Representative images of the change in morphology of healthy CD8$^+$ T cells on ICAM-1 following exposure to IL-2. Cells were fixed and stained with phalloidin-AF488. Colors indicate the intensity of F-actin staining. Scale bar, 20 μm.

(F) PCA plots of average cell morphology for each donor stimulated with ICAM or ICAM/anti-CD3 Abs, built using 5 key morphological parameters (averaged across all samples for each donor). Gray lines connect data points from same donor for IL-2-deprived and IL-2-exposed groups.

(G) Representative blot images for F-actin and G-actin content in one healthy donor following exposure to IL-2 (left).

(H) Total (F+G) actin calculated from the analysis of samples from four healthy donors (error bar represents SD).

(I) F/G-actin ratio calculated from the analysis of samples from four healthy donors (error bar represents SD). Comparable data were obtained in an independent experiment.

One-way ANOVA statistical test was performed for (B), (D), (H), and (I). **p $\leq$ 0.01, ***p $\leq$ 0.001, ****p $\leq$ 0.0001.

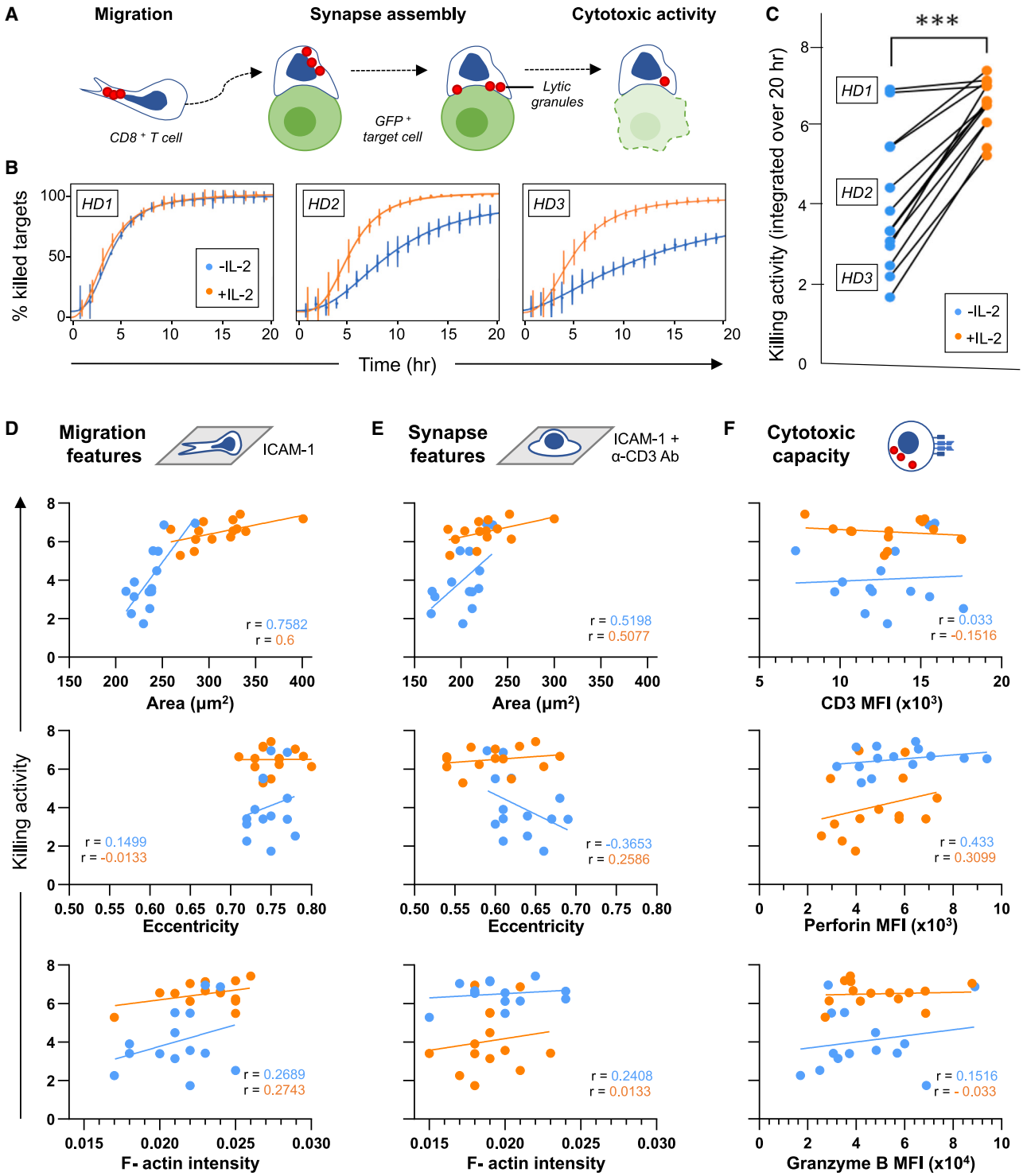

Figure 2. IL-2 stimulates the killing activity of CD8⁺ T cells, which most relates to spreading prowess

(A) Schematic of the dynamic steps leading to the killing of target cells by CD8⁺ T cells.

(B) Kinetics of target cell elimination by CD8⁺ T cells from 3 healthy donors (HDs) under IL-2-deprived and IL-2-exposed conditions, as assessed by video microscopy recording (error bars represent SD of triplicate measurements).

(C) Cytotoxic activity was measured for 14 HD CD8⁺ T cells as the integration of the killing of anti-CD3 Ab-coated P815 target cells over 24 h.

(D) Correlation analysis between integrated killing activity and cell area, eccentricity, and F-actin intensity (mean) for cells from 14 HDs stimulated with ICAM-1.

(legend continued on next page)

(Figure 1I), suggesting that IL-2 not only stimulates actin protein expression but also its polymerization. Combined, these data suggest that the ability of IL-2 to promote morphological fitness in human effector CD8$^+$ T cells under conditions favoring migration and synapse assembly is sustained by a stimulation of actin expression and polymerization.

The cytotoxic activity of effector CD8$^+$ T cells scales with their spreading capability

We next investigated how the morphological fitness of CD8$^+$ T cells might translate into their ability to kill target cells. Since IL-2 is a well-established stimulant of cytotoxicity,[14,15] we used it as a stimulus to investigate the relationship between morphological fitness and effector function. Motility and IS assembly are expected to contribute to killing since they are key features to sustain the search for target cells and contact-dependent delivery of effector molecules. To address this experimentally, we opted for a high-throughput assay to assess the killing kinetics across our collection of cell lines under conditions of limited cell density to challenge both motility and IS assembly (Figure 2A). Killing of target cells was detected after a short lag phase and increased with different rates according to the donors to reach a plateau approaching near-complete elimination of target cells for the most efficient lines (Figure 2B). Except for the 2 T cell lines with the highest killing rate, all T cell lines displayed an increased killing activity upon IL-2 exposure, as indicated by a steadier slope of killing and earlier plateau response (Figure 2B). An integrated killing activity was calculated from the corresponding areas under the curve, highlighting both the inter-individual heterogeneity of killing across the 14 T cell lines and the systematic effect of IL-2 in boosting killing activity (Figure 2C). We next asked whether the killing activity might relate to the key morphological features identified as hallmarks of the inter-individual heterogeneity and effect of IL-2 on morphological fitness. The mean area of the cell spreading over ICAM-1 and, to a lesser extent, the mean area of the cells spreading over ICAM-1/anti-CD3 Abs were identified as features correlating with killing activity both in IL-2-treated and IL-2-deprived T cells (Figures 2D and 2E). Differently, eccentricity and F-actin intensity did not appear to relate to killing activity. Remarkably, expression of CD3, perforin, and granzyme B was not predictive of the killing activity (Figure 2F). The alignment of morphometric data with cytotoxic activity therefore indicates that CD8$^+$ T cell spreading under conditions stimulating migratory behavior and IS assembly is associated with the killing activity of those cells. This finding is in line with the notion that CD8$^+$ T cell-mediated killing depends on the ability of those cells to search for and to establish tight contacts with target cells.

IL-2 promotes morphological fitness by boosting glycolytic activity

We next reasoned that the ability of IL-2 to boost the morphological fitness and associated killing activity in CD8$^+$ T cells might be related to its propensity to raise the energy status of the cells. ATP content was indeed increased in CD8$^+$ T cells upon overnight exposure to IL-2, as measured by the CellTiter-Glo luminescence assay (Figure 3A). In agreement, the global energy status of the cells rose upon IL-2 exposure, as determined by the single cell energetic metabolism profiling translation inhibition (SCENITH) assay, based on the cytometry-based measurement of protein translation with an anti-puromycin Ab[16] as a proxy for metabolic activity (Figure 3B). Using the glucose analog 2-deoxy-D-glucose (2-DG) or the ATP synthase inhibitor oligomycin, which inhibit glycolysis and OXPHOS, respectively, we found that CD8$^+$ T cells relied primarily on glycolysis to produce energy, as expected from effector cells. These data suggest that glycolysis rather than OXPHOS might sustain the morphological fitness of these cells. To directly test whether the IL-2-driven stimulation of glycolysis might contribute to morphological fitness, T cells were exposed to IL-2 in the presence of 2-DG. Exposure to IL-2 alone stimulated T cell elongation on ICAM-1 and radial spreading on ICAM-1/anti-CD3 Abs (Figure 3C). Remarkably, 2-DG almost completely abrogated the IL-2-evoked morphological response, with cells displaying reduced elongation on ICAM-1 and limited non-radial spreading on ICAM-1/anti-CD3 Abs. Quantification of the cell area and F-actin intensity confirmed that the IL-2 evoked potentiation of actin-dependent effector T cell spreading over both stimulatory surfaces was lost upon 2-DG treatment (Figures 3D, 3E, and S6A). These data indicate that the stimulation of glycolysis accounts for the morphological fitness of effector CD8$^+$ T cells upon IL-2 exposure.

IL-2 costimulates the transcription of glycolytic enzymes, actin, and ARP2/3 subunits

The ability of IL-2 to stimulate glycolysis in effector T cells has been shown to be controlled at the transcriptional level.[9,11,17,18] Whether the transcription reprogramming activity of IL-2 impacts additional molecular pathways expected to sustain morphological fitness, such as the cytoskeleton, has not been systematically explored. To address this, we performed a global analysis of the effect of IL-2 on the transcriptome of effector CD8$^+$ T cells. Bulk full-length RNA sequencing (RNA-seq) analysis was applied across the IL-2-deprived and IL-2-exposed effector CD8$^+$ T cells from the healthy donor cohort. IL-2 induced a robust reprogramming of the CD8$^+$ T cell transcriptome, as indicated by the clear segregation of the IL-2-deprived and IL-2-exposed samples (Figure S3A). The glycolytic pathway repressor *BCL6* belonged to the most downregulated genes (Figure S3B), in agreement with the propensity of IL-2 to favor aerobic glycolysis for rapid ATP production in effector CD8$^+$ T cells.[15,19] Among the top upregulated genes were genes involved in membrane lipid biosynthesis (*ENPP6*, *GPR84*, and *SMPD3*), in line with the increased cell spreading ability of IL-2-exposed T cells. A more detailed analysis of the metabolic reprogramming evoked by IL-2 exposure revealed that all 10 enzymes of the glycolytic pathway were upregulated across the 14 tested healthy donor

(E) Correlation analysis between integrated killing activity and cell area, eccentricity, and F-actin intensity (mean) for cells from 14 HDs stimulated with ICAM-1/anti-CD3 Abs.

(F) Correlation analysis between integrated killing activity and CD3, perforin, and granzyme B mean fluorescence intensity (MFI), as assessed by flow cytometry. Paired t test was performed for (C); ***p $\leq$ 0.001. Correlation analysis in (D)–(F) was performed by calculating Spearman's coefficient (r).

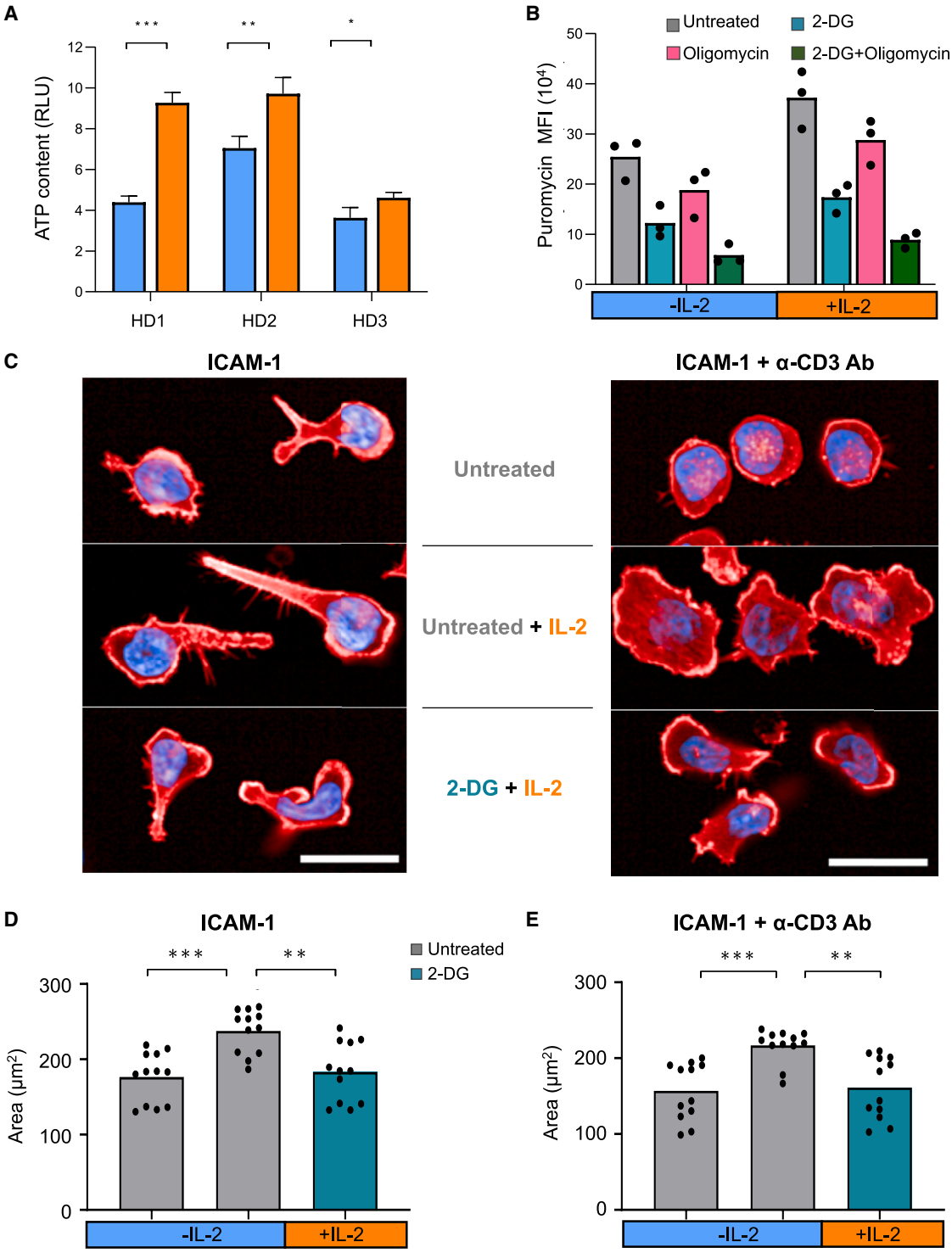

Figure 3. Glycolysis accounts for the ability of IL-2 to stimulate T cell morphological fitness

(A) ATP content as measured in relative luminescence units (RLUs) with the CellTiter-Glo assay. Mean and SD of triplicate measurements for 3 donors are shown. Paired t test comparison test was used for statistical evaluation. *$p \leq 0.05$, **$p \leq 0.01$, ***$p \leq 0.001$.

(B) SCENITH measurement of metabolic activity (flow cytometry assessment of puromycin MFI upon treatment with 2-DG and oligomycin). Each dot represents an HD. Paired t test was used to compare each treatment to the untreated condition. *$p \leq 0.05$, ***$p \leq 0.001$, ****$p \leq 0.0001$.

(C) Morphology displayed by T cells on ICAM-1 or ICAM-1/anti-CD3 Abs after combined treatment with IL-2 and 2-DG, as indicated. Scale bars, 20 μm.

(D and E) Mean area of cells from six HDs stimulated with ICAM-1 (D) or ICAM-1/anti-CD3 Abs (E) and treated with IL-2 and 2-DG as indicated. Duplicate values for each donor are shown. One-way ANOVA comparison test was used for statistical evaluation. **$p \leq 0.01$, ***$p \leq 0.001$.

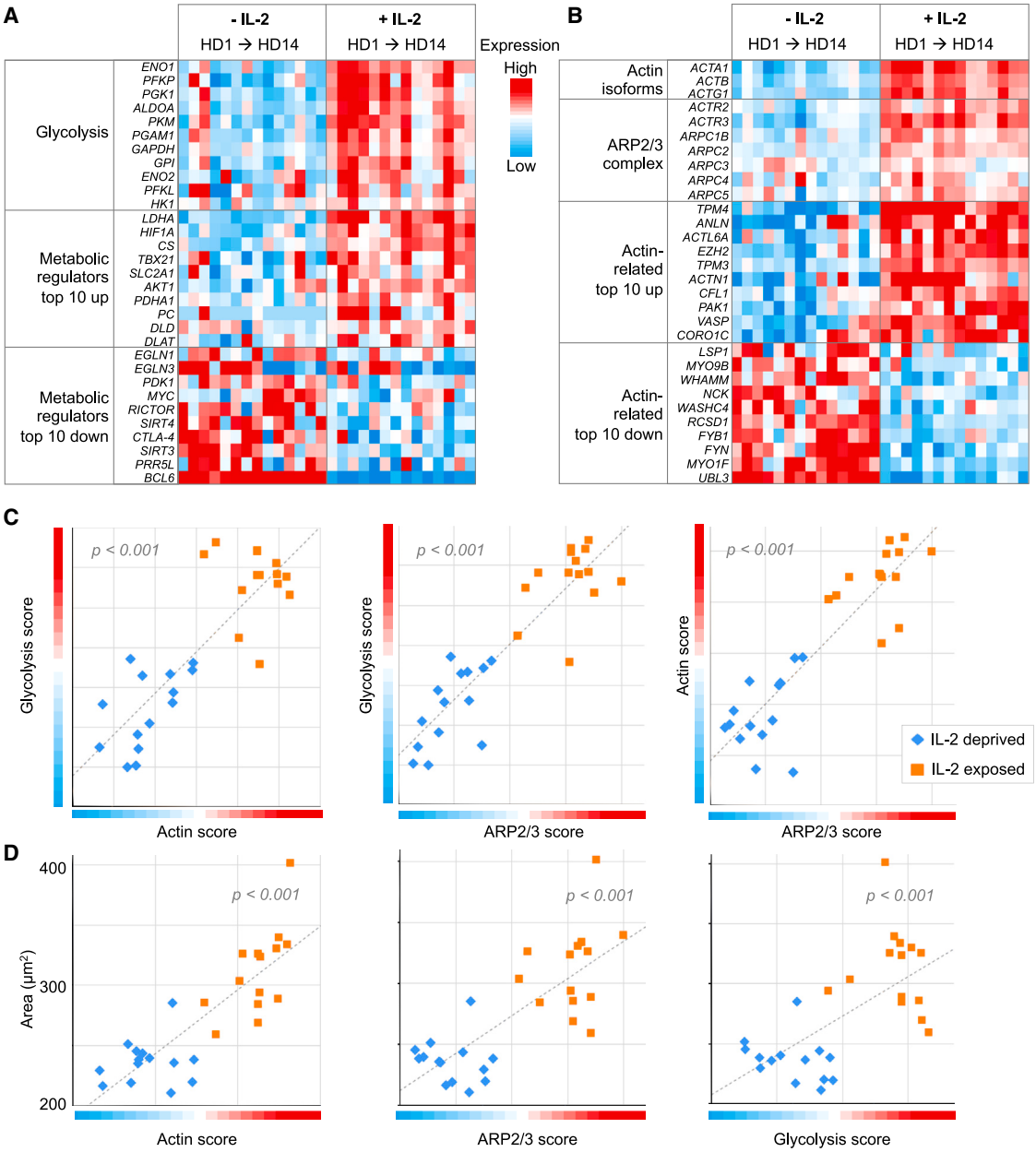

Figure 4. Coordinated transcription of actin and glycolytic pathways relates to spreading capacity

(A) Heatmap of differential expression of genes encoding glycolytic enzymes and metabolic regulators between IL-2-deprived and -exposed CD8$^+$ T cells from 14 HDs.

(B) Heatmap of differential expression of genes encoding actin isoforms and actin-related genes between IL-2-deprived and -exposed HD CD8$^+$ T cells from 14 HDs.

(C) Association between expression of actin, ARP2/3, and glycolytic genes on the individual donor level. Color and shape indicate cells from single HDs deprived of or exposed to IL-2. A gray dotted line indicates linear fit into the cumulative distribution. The p value for each linear fit is indicated.

(D) Association between expression of actin, ARP2/3, and glycolytic genes and spreading of HD CD8$^+$ T cells on ICAM-1 on the individual donor level. Color and shape indicate cells from single donors deprived of or exposed to IL-2. A gray dotted line indicates linear fit into the cumulative distribution. The p value for each linear fit is indicated.

CD8$^+$ T cell samples (Figure 4A). IL-2 also robustly stimulated the transcription of lactate dehydrogenase A (*LDHA*), an enzyme converting pyruvate to lactate to sustain glycolytic flux, which was recently identified as a key regulator of CD8$^+$ T cell function.[20] In accordance with the IL-2-driven stimulation of aerobic glycolysis, genes encoding the transcription factors HIF-1α and t-bet (*TBX21*) as well the glucose transporter GLUT1 (*SLC2A1*) were among the top 10 upregulated metabolism-related genes.

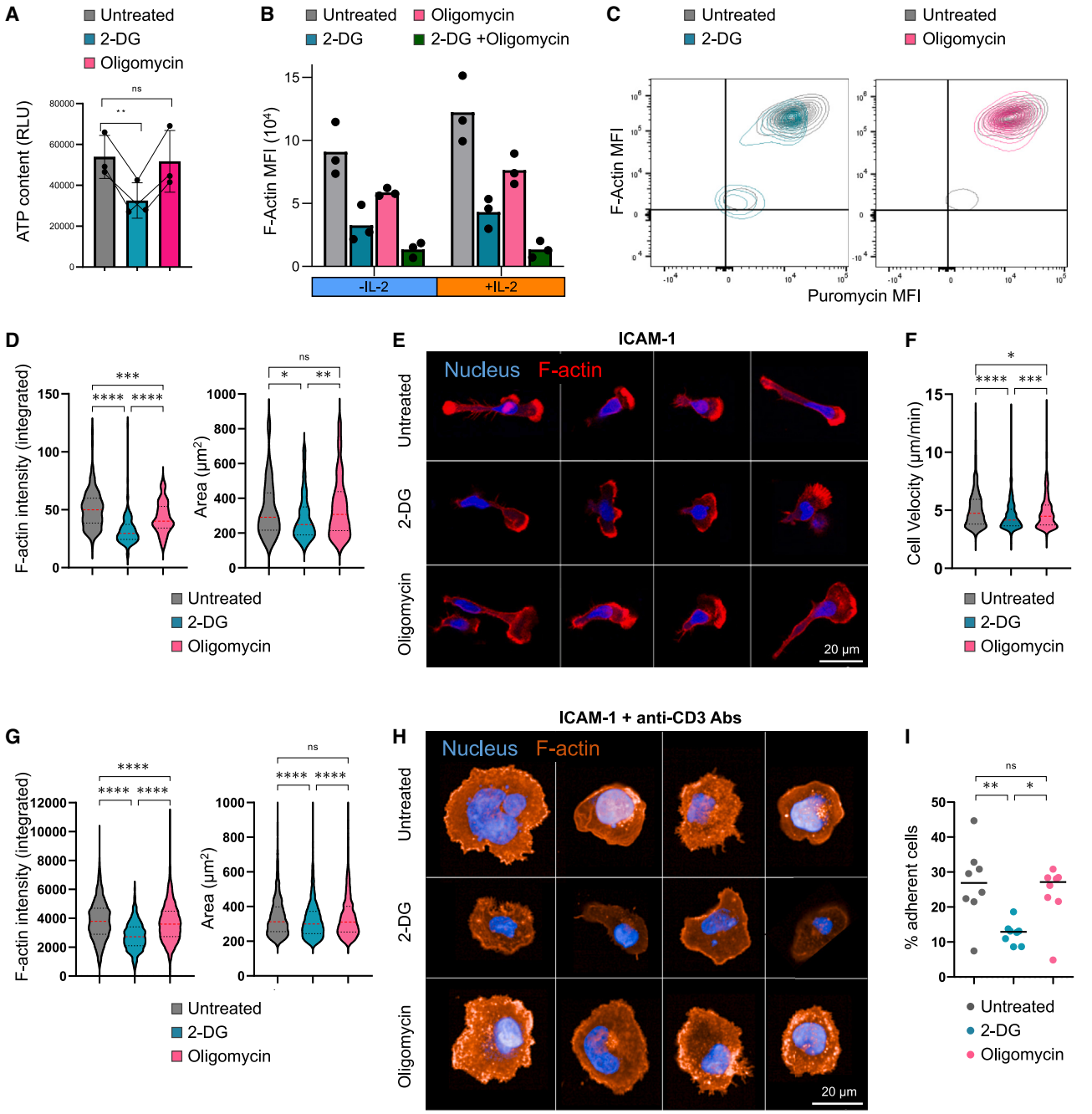

Figure 5. Glycolysis fuels F-actin at the lamellipodium to sustain motility and synapse assembly

(A) ATP content as measured in RLUs with the CellTiter-Glo assay. Mean and SD of triplicate measurements for 3 donors are shown. Paired t test comparison test was used for statistical evaluation. **p $\leq$ 0.01.

(B) Flow cytometry-based measurement of F-actin MFI with phalloidin staining following treatment with 2-DG and oligomycin. One representative experiment with 3 donors is shown, of 2 performed.

(C) Contour plots representing parallel measurements of puromycin and F-actin intensities on cells treated with 2-DG or oligomycin.

(D) Mean F-actin intensity and cell area values extracted from 125 untreated, 155 2-DG-treated, and 137 oligomycin-treated CD8$^+$ T cells seeded on ICAM-1 surfaces.

(E) Representative confocal images of untreated, 2-DG-treated, and oligomycin-treated CD8$^+$ T cells seeded on ICAM-1, fixed and stained with phalloidin and DAPI to reveal F-actin and nuclei, respectively. Scale bar, 20 μm.

(F) Migration velocity of CD8$^+$ T cells upon interaction with coated ICAM-1. Data were extracted from 328 untreated, 512 2-DG-treated, and 648 oligomycin-treated CD8$^+$ T cells.

(legend continued on next page)

Furthermore, the mitochondrial enzymes and cofactors that convert pyruvate to acetyl-coenzyme A (CoA) (*PDHA1* and *DLAT*) and oxaloacetate (*PC*) to feed the tricarboxylic acid (TCA) cycle as well as the TCA cycle enzyme citrate synthase *(CS)* were upregulated. However, systematic analysis of the effect of IL-2 stimulation on the TCA cycle and mitochondrial OXPHOS revealed a partial remodeling activity, where only a portion of the related genes were upregulated (Figure S4). Therefore, while IL-2 robustly stimulates the glycolytic pathway at the transcriptional level, it appears to remodel the TCA cycle and mitochondrial OXPHOS pathways via variable transcriptional regulation of their components.

Our RNA-seq analysis further indicated IL-2-dependent transcriptional reprogramming of the actin-remodeling machinery of effector $CD8^+$ T cells (Figure 4B). Upregulated genes included the actin isoforms *ACTA1*, *ACTB*, and *ACTG1*, in agreement with the finding that IL-2 stimulated global actin protein content. Upregulated genes also included profilin (*PFN1*), converting monomeric ADP/G-actin to ATP/G-actin; ARP2/3 complex subunits (*ACTR2*, *ACTR3*, *ARPC1B*, *ARPC2*, and *ARPC5*); multiple actin-binding proteins known to regulate actin network stability and turnover (*ANLN*, *ACTN1*, *ACTN4*, *CFL1*, *TPM3*, *TPM4*, *VASP*, and *WDR1*); as well as upstream regulators (*CDC42*, *PAK1*, and *RHOA*). In opposition, IL-2 exposure caused the downregulation of genes encoding a more restricted set of actin-related molecules, including HEM1 (*NCKAP1L*), the WASP-interacting protein (*WIPF1*), the WASP-related protein complex WASH (*WASHC1*, *WHASHC2C*, *WASHC3*, and *WHASHC4*) and WHAMM (*WHAMM*), as well as myosin motors (*MYO1F* and *MYO9B*) and LSP1, a key regulator of actomyosin contractility. This RNA-seq analysis, together with the F-actin and G-actin content measurements, strongly suggest that IL-2 promotes actin expression and stimulates its polymerization via a molecular program including the ARP2/3 complex.

We next sought to exploit the inter-individual variability in gene expression among the considered donors to interrogate whether some aspects of the metabolic and actin cytoskeleton programs might be co-regulated. Correlation analysis across the 28 analyzed samples was performed by aligning the gene expression scores (STAR Methods) pertaining to the actin cytoskeleton machinery on one side (actin isoforms and ARP2/3 components) and to the metabolic activity on the other side. Positive correlation was identified between the expression of actin and glycolysis-related genes (Figure 4C), suggesting that IL-2 stimulates a coordinated transcriptional program, resulting in the alignment of the actin machinery responsible for branched F-actin networks and rapid ATP production via glycolysis. We then took advantage of the fact that the RNA-seq analysis was conducted in parallel to the morphological profiling by HCI to investigate how the co-regulated expression of genes pertaining to the actin machinery and the glycolytic pathway might relate to the morphological fitness across the considered samples. Cell area and pathway activation scores were used as proxies for cell morphology and pathway activity, respectively (Figure 4D). Expression of actin isoform genes (*ACTA1*, *ACTB*, and *ACTG1*), ARP2/3 genes (*ACTR2*, *ACTR3*, *ARPC1B*, *ARPC2*, and *ARPC5*) and genes encoding glycolytic enzymes *(ALDOA*, *ENO1*, *ENO2*, *GAPDH*, *GPI*, *HK1*, *PFKL*, *PFKP*, *PGAM1*, *PGK1*, and *PKM)* were found to correlate positively with the spreading of T cells from individual donors. Collectively, our results are suggestive of a co-regulation between glycolysis and actin remodeling to set the effector fitness of $CD8^+$ T cells.

Glycolysis sustains lamellipodial F-actin during migration and synaptic adhesion

To assess the reliance of effector T cells on glycolysis and mitochondrial OXPHOS to produce ATP and fuel actin polymerization for motility and IS assembly, cells were treated with the glucose analogue 2-DG, the glycolysis-inhibiting drugs shikonin (an inhibitor of pyruvate kinase) and 3-bromopyruvate (an inhibitor of phosphofructokinase), the lactate dehydrogenase inhibitor galloflavin, or the OXPHOS-targeting drugs oligomycin, antimycin A, carbonylcyanid-4-(trifluromethoxy)phenylhydrazone (FCCP), and rotenone (see depictions of the drug targets in Figures S7A and S8A). While treatment with 2-DG, shikonin, and 3-bromopyruvate significantly reduced ATP production, treatment with galloflavin or any of the OXPHOS drugs did not, confirming that effector T cells highly depend on glycolysis for energy production (Figures 5A, S7B, and S8B). Flow cytometry quantification of fluorescent phalloidin showed that 2-DG treatment resulted in a stronger drop of F-actin content than treatment with oligomycin (Figure 5B), mirroring the effect of these drugs on the energy status of the cells (Figure 3B). We further made use of the SCENITH method to assess, in parallel, metabolic activity and F-actin content with single-cell resolution. Our analysis indicates that treatment with 2-DG, but not with oligomycin, induced a parallel decline in metabolic activity and F-actin content (Figure 5C), supporting the notion that F-actin polymerization in effector T cells scales with the level of ATP provided through glycolysis. The observation that 2-DG treatment also reduced the phosphorylation of signaling molecules evoked by the stimulation through LFA-1 and the TCR (Figure S5) indicates that glycolysis may control actin remodeling directly by fueling F-actin polymerization but also indirectly by controlling signaling activity, as recently established.[20] We then turned back to quantitative cell imaging to directly assess the effect of glycolysis- and mitochondrial OXPHOS-targeting drugs on F-actin content and distribution in the context of motility and IS assembly. Upon stimulation on coated ICAM-1, untreated cells adopted an elongated morphology with an F-actin-rich lamellipodium at the leading

(G) Mean F-actin intensity and cell area values were extracted from 2,737 untreated, 1,325 2-DG-treated, and 2,526 oligomycin-treated $CD8^+$ T cells upon interaction with ICAM-1 and anti-CD3 Abs. Shown are pooled data of 2 independent experiments.
(H) Representative confocal images of untreated, 2-DG-treated, and oligomycin-treated $CD8^+$ T cells seeded on ICAM-1 and anti-CD3 Abs, fixed and stained with phalloidin and DAPI to reveal F-actin and nuclei, respectively. Scale bar, 20 μm.
(I) Adhesion of $CD8^+$ T cells over ICAM-1 and anti-CD3 Abs was quantified in 8 replicates stemming from 2 experiments.
Paired t test was used for statistical evaluation of data in (A). Tukey's multiple-comparisons test was used for statistical evaluation of data in (B), (D), (F), (G), and (I). ns, $p > 0.05$; *$p \leq 0.05$; **$p \leq 0.01$; ***$p \leq 0.001$; ****$p \leq 0.0001$.

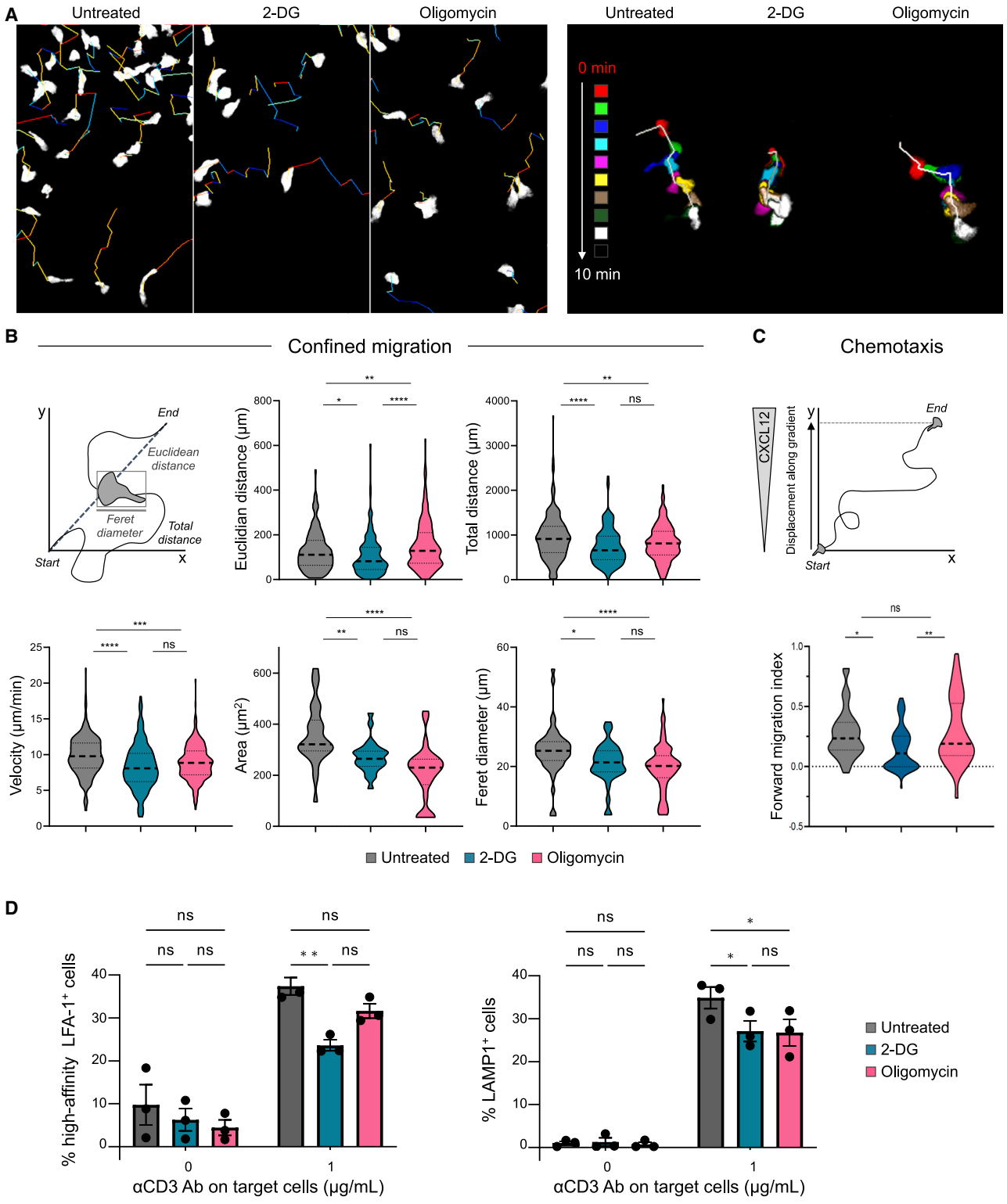

Figure 6. 2-DG and oligomycin impact confined migration and degranulation of CD8⁺ T cells

(A) Representative snapshots of untreated and 2-DG- and oligomycin-treated CD8⁺ T cells migrating in a confined environment (under agarose) that included an ICAM-1 coating and soluble CXCL12 (left). The tracks behind the cells represent the last 10 min of their displacement. Colors reflect the instant directionality along the CXCL12 gradient. Shown are morphological contours of representative untreated and 2-DG-treated and oligomycin-treated cells along 10-min tracks (right, same settings as in A).

(legend continued on next page)

edge, while T cells treated with 2-DG and other glycolysis-inhibiting drugs displayed decreased spreading, lower polarization, and reduced F-actin density at the lamellipodium (Figures 5D, 5E, and S7C). Although lactate has been shown recently to sustain the anti-tumor function of CD8$^+$ T cells,[21,22] inhibition of lactate dehydrogenase had no impact on cell area and F-actin intensity (Figure S7C). This indicates that production of ATP, rather than production of the metabolic intermediate lactate, is the major of energy by which glycolysis sustains actin remodeling during the activation of effector T cells. Inhibition of OXPHOS resulted in a less pronounced reduction of F-actin density and did not impact cell area (Figures 5D, 5E, and S8C). Analysis of migration capacity by live microscopy showed reduced velocity in cells treated with 2-DG compared with untreated cells or cells treated with oligomycin (Figure 5F). The dependency of effector CD8$^+$ T cells on glycolysis vs. mitochondrial activity to assemble an adhesive synapse was then tested by treating cells with 2-DG or OXPHOS-targeting drugs and seeding them over ICAM-1/anti-CD3 Ab-coated surfaces. Confocal image analysis revealed that treatment of cells with 2-DG and other glycolysis-inhibiting drugs was associated with strongly reduced F-actin density at the adhesion plane, while OXPHOS-targeting drugs had a modest effect (Figures 5G, 5H, S7D, and S8D). Moreover, only the blockage of glycolysis resulted in a reduction of synapse area (Figures 5G, S7D, and S8D) and of the proportion of cells able to firmly adhere to the ICAM-1/anti-CD3 Ab-coated surface (Figure 5I). Together, these data indicate that glycolysis represents the major source of ATP to sustain actin branching at the lamellipodium in the context of effector CD8$^+$ T cell migration and synaptic adhesion, while mitochondrial OXPHOS might govern a relatively limited actin-remodeling activity in the context of migration.

Glycolysis and mitochondrial OXPHOS distinctly contribute to migration and adhesion to target cells

The reliance of effector CD8$^+$ T cells on energy production via glycolysis and mitochondrial OXPHOS for actin-dependent activities was further examined in the context of confined migration and chemotaxis. Both 2-DG and oligomycin treatments affected the ability of CD8$^+$ T cells to migrate under confinement, as assessed in an under-agarose migration setting. While 2-DG strongly reduced the exploratory behavior of the cells and their net displacement, oligomycin appeared to mostly reduce the length of the tracks (Figure 6A). Examination of cell shape dynamics indicated that, while untreated cells migrated by alternating phases of elongation and retraction, 2-DG-treated cells displayed reduced shape remodeling, in accordance with their confined behavior (Figure 6B). Oligomycin-treated cells displayed a reduced ability to elongate and retract, in accordance with their reduced velocity. Further analysis of cell shape parameters indicated that 2-DG-treated cells were unable to maintain an elongated morphology. Although oligomycin-treated cells had less pronounced defects in confined migration compared with 2-DG-treated cells, they displayed a marked reduction in cell spreading and elongation. These data therefore reveal that glycolysis and mitochondrial OXPHOS contribute in different ways to confined migration. While glycolysis might sustain confined migration by promoting actin branching at the lamellipodium, mitochondrial OXPHOS might promote a separate actin pool involved in contractility, as suggested previously.[6] The effects of 2-DG and oligomycin were further tested in the context of a linear gradient of CXCL12 using dedicated chemotaxis chambers. Interestingly, directional migration, as measured by the forward migration index, was severely reduced in 2-DG-treated cells, while their velocity was reduced nearly 2-fold. In contrast, oligomycin-treated cells displayed a preserved ability to migrate directionally in this setting (Figure 6C). This reinforces the notion that glycolysis would be particularly required to sustain exploration and gradient orientation. The effects of 2-DG and oligomycin were then examined in the context of IS assembly with target cells. Staining for high-affinity LFA-1 in conjugates formed between effector T cells and P815 target cells coated with anti-CD3 Abs was used as a molecular marker for tight adhesion (Figure 6D). Treatment with 2-DG, but not with oligomycin, was found to significantly reduced LFA-1 conformational activation, confirming the higher dependency of effector T cells on glycolysis to assemble an adhesive IS. Lytic granule exocytosis, as measured by surface LAMP-1 staining, was modestly and comparably affected by 2-DG and oligomycin treatment, suggesting that this activity is less prominently dependent on active glycolysis and OXPHOS. Collectively, these data indicate that glycolysis is required for confined migration and IS assembly by effector CD8$^+$ T cells, in line with the key role of this pathway in ATP production and sustainment of the actin-rich lamellipodium. Although mitochondrial OXPHOS accounts for a limited fraction of ATP in these cells, it appears to be particularly required for optimizing motility under confinement.

The role of ARP2/3 and upstream regulators in controlling the morphological and functional fitness of cytotoxic T cells

Our findings show that, upon exposure to IL-2, effector T cells activate a coordinated transcriptional program of glycolysis and actin remodeling. They also indicate that, during motility and IS assembly, glycolysis is required to sustain actin remodel-

(B) Velocity, total distance, and Euclidean distance were extracted from 320 untreated and 161 2-DG- and 268 oligomycin-treated cells. Cell area and Feret diameter were extracted from 51 untreated and 36 2-DG- and 103 oligomycin-treated cells. Data from one representative under-agarose migration experiment of 3 are displayed.

(C) Forward migration index (defined as the ratio of displacement along the y axis to total distance; see scheme) was extracted from 40 untreated and 73 2-DG- and 41 oligomycin-treated cells that were exposed to a CXCL12 gradient in dedicated chemotaxis chambers. Tukey's multiple-comparisons tests were used for statistical evaluation of data presented in (B) and (C). ns, $p > 0.05$; *$p \leq 0.05$; **$p \leq 0.01$; ***$p \leq 0.001$; ****$p \leq 0.0001$.

(D) Percentage of cells detected as positive for high-affinity LFA-1 (left) and LAMP1 (right) by flow cytometry. CD8$^+$ T cells were pretreated with 2-DG or oligomycin as indicated and co-cultured with P815 target cells coated or not coated with anti-CD3 Abs. Data represent a pool of 3 independent experiments. two-way ANOVA significance tests were used. ns, $p > 0.05$; *$p \leq 0.05$; **$p \leq 0.01$.

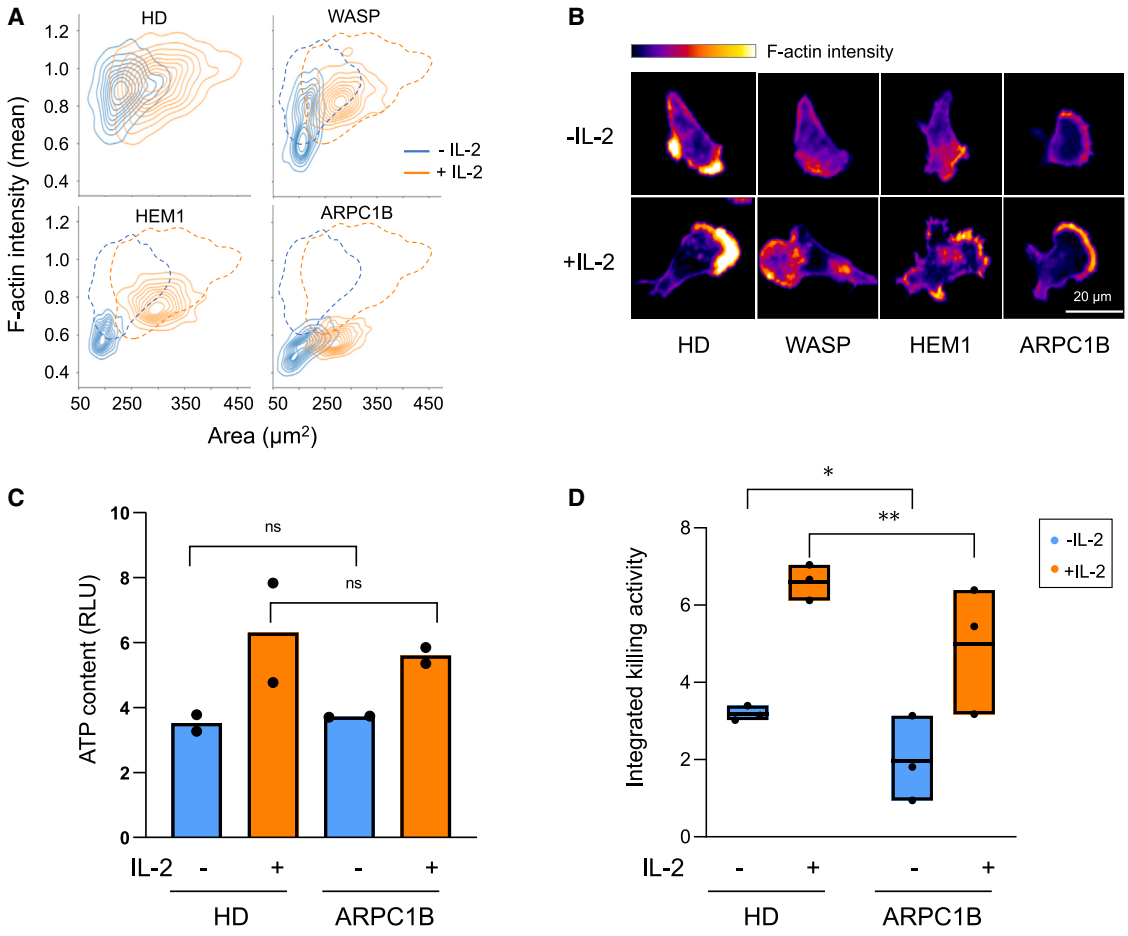

Figure 7. IL-2-evoked morphological and functional fitness is dependent on ARPC1B

(A) Density plots of changes in T cell morphology on ICAM-1 for IL-2-deprived or -exposed CD8$^+$ T cells from three HDs, three patients with WASP deficiency, two patients with HEM1 deficiency, and three patients with ARPC1B deficiency.

(B) Representative images of healthy and ARPC1B-, HEM1- and WASP-deficient CD8$^+$ T cells on ICAM-1 following IL-2 deprivation or exposure. The color scale represents the intensity of F-actin staining with phalloidin-AF488. Scale bar, 20 μm.

(C) ATP content as measured in RLUs with the CellTiter-Glo assay. Mean for two HDs and two ARPC1B patients are shown. Paired t test comparison test was used for statistical evaluation. ns, $p > 0.05$.

(D) Integrated killing activity of three HDs and three ARPC1B patients following IL-2 deprivation or exposure. Paired t test comparison test was used for statistical evaluation. *$p \leq 0.05$, **$p \leq 0.01$.

ing at the lamellipodium, possibly by fueling actin polymerization. Given the well-established role of the ARP2/3 complex in promoting actin branching at the lamellipodium and, here, the measured activation of its transcription by IL-2, we next examined the contribution of ARP2/3-dependent actin remodeling in mediating the IL-2-driven morphological and functional fitness. For that purpose, we examined untransformed CD8$^+$ T cells derived from patients with characterized deficiencies in the ARPC1B subunit of the ARP2/3 complex and in the ARP2/3 activators HEM1 and WASP (Figures S6A–S6C). Such an evaluation in patient-derived material was further motivated by a previous indication of an IL-2corrective effect in WASP-deficient natural killer (NK) cells.[23,24] HCI-based analysis showed that, upon stimulation over ICAM-1, T cells from patients with germline-encoded deficiencies of ARPC1B, HEM1, and WASP harbored prominent morphological defects. In cells deficient for either of the three aforementioned actin regulators, T cells were detected to have reduced F-actin density at the adhesion plane, associated with reduced spreading (Figure 7A). This combined defect appeared to be most pronounced in ARPC1B deficiency, intermediate in HEM1 deficiency, and milder in WASP deficiency. HEM1- and ARPC1B-deficient T cells emitted a very thin F-actin-rich lamellipodium, if any, while WASP-deficient T cells still emitted a lamellipodium, which, however, harbored reduced F-actin density (Figure 7B). Our analysis further highlighted that exposure of patient-derived T cells to IL-2 significantly increased their responsiveness to ICAM-1 (Figures 7A and 7B). However, while the F-actin and cell spreading parameters reached values overlapping the low normal range for WASP- and HEM1-deficient T cells, these parameters remained at abnormally low values for ARPC1B-deficient T cells. This comparative analysis therefore indicates that ARPC1B, HEM1,

and WASP deficiencies are associated with different degrees of actin-dependent spreading over ICAM-1 that can be partially corrected by exogenous IL-2. The severe defect observed in ARPC1B-deficient T cells highlights the requirement of an ARPC1B-containing ARP2/3 complex in governing lamellipodium assembly in T cells.

We next focused on the ARPC1B-deficient T cells to investigate whether their actin-related defect might be associated with reduced ATP production. However, both basal and IL-2-evoked ATP contents were comparable with those observed in healthy donor T cells (Figure 7C), implying that the energy status of ARPC1B-deficient T cells did not account for their morphological defects. Given our identification of cell spreading as a key parameter to sustain efficient killing, we monitored the killing activity of ARPC1B-deficient $CD8^+$ T cells. As reported previously, these cells displayed reduced cytotoxic activity, as tested over a 20-h co-culture with anti-CD3 Ab-coated P815 cells (Figure 7D). Although exposure to IL-2 stimulated the killing activity of these cells, they failed to reach normal killing activity. Collectively, these data reinforce the position of the ARP2/3 complex as a pivotal controller of the morphological and functional fitness of cytotoxic T cells. They further suggest that the activity of the IL-2-glycolysis-ATP axis is maintained in ARPC1B-deficient T cells but that it is not sufficient to stimulate normal morphology and function because of the reduced properties of the ARP2/3 complex in the context of ARPC1B deficiency.

DISCUSSION

Although T cells adopt typical morphologies to execute different steps of their immune surveillance activity, features describing these morphologies remain poorly exploited in studies of T cell biology. By combining HCI and bulk RNA-seq on a collection of effector $CD8^+$ T cells from healthy donors and actinopathy patients, we provide insight into the molecular and metabolic determinants of $CD8^+$ T cell actin cytoskeleton remodeling and related morphological fitness. Our screen reveals distinct $CD8^+$ T cell morphological signatures associated with deficiencies in ARP2/3-related molecules. It further indicates that the propensity of effector $CD8^+$ T cells to remodel their morphology scales with the transcriptional regulation of glycolytic enzymes, actin isoforms, and ARP2/3 subunits. It also points to glycolysis as the major source of ATP to drive actin polymerization at the lamellipodium and related sustainment of motility, IS assembly, and cytotoxic activity.

Using IL-2 as a natural stimulator of T cell function, we observe interplay between the energetic state of effector $CD8^+$ T cells and their ability to engage in actin-driven motility and IS assembly. We show that IL-2 stimulation of $CD8^+$ T cells leads to a drastic boost of cell morphology under conditions eliciting migration or IS formation. Interestingly, IL-2 appears to affect the actin cytoskeleton both quantitatively by upregulating global cellular content in actin and qualitatively by raising the proportion of F-actin and promoting lamellipodium assembly. These IL-2 effects are mirrored at the transcriptional level by the propensity of IL-2 to upregulate not only the genes encoding actin isoforms but also to preferentially upregulate actin regulators directly involved in lamellipodium assembly, such as the ARP2/3 complex. Activation of the transcription of cytoskeleton genes by IL-2 agrees with analysis of the proteome of IL-2-exposed murine T cells[25] and indicates the key role of actin remodeling in IL-2-induced boosting of T cell function.

In parallel with revealing the activation of an actin remodeling program, our RNA-seq analysis confirms previously reported IL-2-induced activation of cell glycolysis.[26,27] It further reveals a correlation of actin branching regulation and glycolytic potential at the transcriptional level, which indicates that T cells align activation of their actin-nucleating machinery and their ATP production capacity via glycolysis. These findings fit the proposed notion of a synchronization between metabolic and functional programs in T cells along their differentiation path.[28] Although 2-DG has been shown previously to reduce T cell cytotoxic activity[29,30] and cytokine-induced regulatory T cell migration,[31] the effect of 2-DG on actin cytoskeleton organization in T cells has not been evaluated. Our study highlights that glycolysis blockade in effector $CD8^+$ T cells results in a reduction of lamellipodium thickness, IS adhesion, cell migration, and orientation during confined chemotaxis. These data therefore indicate that rapid ATP production via glycolysis sustains ARP2/3-driven actin branching, possibly by directly fueling actin polymerization but also by tuning signaling upstream of ARP2/3 activation. Although mitochondrial OXPHOS appeared to account minimally for global cellular ATP content in our effector T cells, it contributed to F-actin content and quite specifically to cell elongation in the context of confined motility, in agreement with previous observations.[6,32] This raises the possibility of a complex interplay between different energy sources and actin remodeling, whereby glycolysis and mitochondrial OXPHOS might impact distinct pools of actin remodeling to control lamellipodium dynamics, as highlighted here for glycolysis, or uropod contraction, as suggested earlier.[6] Whether ATP production might be spatially constrained to directly fuel local F-actin networks, as described in the context of *C. elegans* invasion,[33,34] will need to be further investigated in the context of T cells.

The comparative analysis of patient-derived T cells confirms previous studies on the corresponding deficiencies[35–39] and further highlights that defects in the closely related actin regulators ARPC1B, HEM1, and WASP are associated with non-overlapping morphological defects. Our results support the view that the WASP family Verprolin homolog (WAVE) complex, to which HEM1 belongs, and WASP are controlling T cell morphological response in a complementary fashion.[40–43] The amelioration of morphological features in cells from patients with actin defects following stimulation with IL-2 is in agreement with previous findings of IL-2's ability to promote F-actin reorganization in WASP-deficient NK cells.[23,24] Our data on ARPC1B-deficient T cells further indicate that these cells have a preserved ability to produce ATP production and are able to enhance actin remodeling upon IL-2 stimulation. However, their ability to spread and their cytotoxic function remain suboptimal, most probably because the integrity of the ARPC1B-containing ARP2/3 complex remains essential and cannot be bypassed by the IL-2 stimulation. The possibility that the major rise in the F/G-actin ratio observed after IL-2 stimulation is driven by the ARP2/3 complex is supported by the previous finding in primary mammary epithelial cells that the S418D ARP3 phospho-mimicking mutant leads to

a rise in F-actin-to-G-actin ratio comparable with the one we measured upon IL-2 stimulation.[44]

In conclusion, our analysis shows that the morphological fitness of effector CD8$^+$ T cells is adjusted via the transcriptional regulation of glucose-dependent ATP production and the ARP2/3-related actin-remodeling machinery. This knowledge opens perspectives not only for the considered actinopathies but also for the optimization of T cell-centered immunotherapy applications. Indeed, metabolic reprogramming via cytokines, nutrients, or drugs currently considered to boost T cell function in the context of infection and cancer would be expected to be mediated, at least in part, via the tuning of actin cytoskeleton dynamics to sustain motility and target cell encounters. In this context, the analytical pipeline implemented in this work might prove useful to screen candidate compounds on primary T cells.

Limitations of the study

Our study highlights individual heterogeneity in the fitness of T cells across the 14 healthy donors studied. Although we exploited this heterogeneity to relate morphological fitness to functional activity and to expression of actin and metabolic programs, our cohort was too limited in size to explore the potential impact of factors such as age, health conditions, sex, etc. Our study highlights the transcriptional upregulation of the Arp2/3 subunits upon IL-2 stimulation. The fact that the nucleation-promoting factors upstream of Arp2/3 are not upregulated suggests that the latter might be activated via alternative mechanisms that were not investigated here. Our study focuses on the impact of ATP production on actin remodeling via glycolysis. In turn, the actin cytoskeleton may provide spatial and functional regulation of glycolysis through binding of glycolytic enzymes to actin,[45] a scenario that would be worth investigating in the context of T cell activation. The interpretation of some of our data relies on the assumption that actin remodeling represents a high energetic cost in terms of ATP consumption.[5] The concept that ATP availability may be a rate-limiting factor for actin remodeling has recently been questioned,[46] pointing to the importance of further investigating the actual ATP cost of actin remodeling in the context of T cell function.

STAR★METHODS

Detailed methods are provided in the online version of this paper and include the following:

- KEY RESOURCES TABLE
- RESOURCE AVAILABILITY
  - Lead contact
  - Materials availability
  - Data and code availability
- EXPERIMENTAL MODEL AND STUDY PARTICIPANT DETAILS
  - Patients
  - Library of patient-derived CD8$^+$ T cells
- METHOD DETAILS
  - Phenotypic characterization of the effector CD8$^+$ T cells
  - Analysis of protein expression
  - High-content stimulation and staining of T cells
  - High-content image acquisition and processing
  - T cell morphology, adhesion, and motility upon treatment with glycolysis and OXPHOS inhibitors
  - Metabolic status with the SCENITH assay
  - Kinetics of cytotoxic activity
  - Assessment of degranulation by cytometry
  - RNA sequencing and raw data processing
  - Transcriptome analysis
  - ATP content measurement with CellTiter-Glo assay
  - Measurement of G-actin and F-actin contents in T cells
  - T cell morphology upon treatment with glycolytic inhibitors and OXPHOS inhibitors
- QUANTIFICATION AND STATISTICAL ANALYSIS

SUPPLEMENTAL INFORMATION

Supplemental information can be found online at https://doi.org/10.1016/j.celrep.2024.113853.

ACKNOWLEDGMENTS

The authors thank Sophie Allart and Simon Lachambre from the cell imaging facility of INFINITy and Raphaëlle Romieu-Mourez and Pierre-Emmanuel Paulet from the immuno-monitoring facility of INFINITy. We thank Giulio Superti-Furga for access to the flow cytometry and high-content cell imaging facilities of the Research Center for Molecular Medicine of the Austrian Academy of Sciences (CeMM). We thank Stefan Kubicek from CeMM for access to the high-content cell-handling facilities. We thank Christoph Bock and his team from the biomedical sequencing facility of CeMM and the Medical University of Vienna for the RNA-seq work. We thank Sevgi Kostel Bal and Michael J. Kraakman for assistance with the SCENITH assay. We thank Nicolas Socquet-Juglard and Pauline Smilovici for assistance with drug treatments and ATP measurements. We thank Ruth Dingelmaier Hovorka for assistance with actin content measurements. We also thank Alessandro Aiuti, Marco Gattorno, and Stefano Volpi for patient-derived cell lines. We thank Renaud Lesourne and Nicolas Destainville for helpful discussions. This work was supported by the Vienna Science and Technology Fund (WWTF-LS16-060 to K.B., J.M., and L.D.), the Austrian Science Fund (FWF stand-alone project P 34118-B to L.D.), and the French National Center for Scientific Research (CNRS International Research Project SysTact to L.D.). For open access purposes, the author has applied a CC BY public copyright license to any author-accepted manuscript version arising from this submission.

AUTHOR CONTRIBUTIONS

A.K. contributed to the design of the research, performed experiments, designed the analytical pipeline, analyzed data, and wrote the paper. T.M. also contributed to the design of the research, performed experiments, analyzed data, and wrote the paper. M.W. contributed to the research design and analyzed data. B.C., C.L., A.-K.M., and L.E.S. performed experiments and analyzed data. M.C. contributed to the image analysis pipeline. J.M., W.P.W., M.F., and K.B. participated in research design and scientific discussions. L.D. designed the research, supervised the analysis pipeline, and wrote the paper.

DECLARATION OF INTERESTS

The authors declare no competing interests.

Received: March 30, 2022
Revised: November 27, 2023
Accepted: February 7, 2024
Published: February 28, 2024

REFERENCES

1. Pollard, T.D., and Cooper, J.A. (2009). Actin, a central player in cell shape and movement. Science (New York, N.Y.) *326*, 1208–1212. https://doi.org/10.1126/science.1175862.
2. Dustin, M.L. (2004). Stop and go traffic to tune T cell responses. Immunity *21*, 305–314. https://doi.org/10.1016/j.immuni.2004.08.016.
3. Weninger, W., Biro, M., and Jain, R. (2014). Leukocyte migration in the interstitial space of non-lymphoid organs. Nat. Rev. Immunol. *14*, 232–246. https://doi.org/10.1038/nri3641.
4. Kamnev, A., Lacouture, C., Fusaro, M., and Dupré, L. (2021). Molecular Tuning of Actin Dynamics in Leukocyte Migration as Revealed by Immune-Related Actinopathies. Front. Immunol. *12*, 750537. https://doi.org/10.3389/fimmu.2021.750537.
5. Bernstein, B.W., and Bamburg, J.R. (2003). Actin-ATP hydrolysis is a major energy drain for neurons. J. Neurosci. *23*, 1–6. https://doi.org/10.1523/jneurosci.23-01-00002.2003.
6. Campello, S., Lacalle, R.A., Bettella, M., Mañes, S., Scorrano, L., and Viola, A. (2006). Orchestration of lymphocyte chemotaxis by mitochondrial dynamics. J. Exp. Med. *203*, 2879–2886. https://doi.org/10.1084/jem.20061877.
7. Baixauli, F., Martín-Cófreces, N.B., Morlino, G., Carrasco, Y.R., Calabia-Linares, C., Veiga, E., Serrador, J.M., and Sánchez-Madrid, F. (2011). The mitochondrial fission factor dynamin-related protein 1 modulates T-cell receptor signalling at the immune synapse. The EMBO journal *30*, 1238–1250. https://doi.org/10.1038/emboj.2011.25.
8. Buck, M.D., O'Sullivan, D., Klein Geltink, R.I., Curtis, J.D., Chang, C.H., Sanin, D.E., Qiu, J., Kretz, O., Braas, D., van der Windt, G.J.W., et al. (2016). Mitochondrial Dynamics Controls T Cell Fate through Metabolic Programming. Cell *166*, 63–76. https://doi.org/10.1016/j.cell.2016.05.035.
9. Finlay, D.K., Rosenzweig, E., Sinclair, L.V., Feijoo-Carnero, C., Hukelmann, J.L., Rolf, J., Panteleyev, A.A., Okkenhaug, K., and Cantrell, D.A. (2012). PDK1 regulation of mTOR and hypoxia-inducible factor 1 integrate metabolism and migration of CD8+ T cells. J. Exp. Med. *209*, 2441–2453. https://doi.org/10.1084/jem.20112607.
10. Gubser, P.M., Bantug, G.R., Razik, L., Fischer, M., Dimeloe, S., Hoenger, G., Durovic, B., Jauch, A., and Hess, C. (2013). Rapid effector function of memory CD8+ T cells requires an immediate-early glycolytic switch. Nat. Immunol. *14*, 1064–1072. https://doi.org/10.1038/ni.2687.
11. Ross, S.H., and Cantrell, D.A. (2018). Signaling and Function of Interleukin-2 in T Lymphocytes. Annu. Rev. Immunol. *36*, 411–433. https://doi.org/10.1146/annurev-immunol-042617-053352.
12. German, Y., Vulliard, L., Kamnev, A., Pfajfer, L., Huemer, J., Mautner, A.K., Rubio, A., Kalinichenko, A., Boztug, K., Ferrand, A., et al. (2021). Morphological profiling of human T and NK lymphocytes by high-content cell imaging. Cell Rep. *36*, 109318. https://doi.org/10.1016/j.celrep.2021.109318.
13. Ross, S.H., Rollings, C., Anderson, K.E., Hawkins, P.T., Stephens, L.R., and Cantrell, D.A. (2016). Phosphoproteomic Analyses of Interleukin 2 Signaling Reveal Integrated JAK Kinase-Dependent and -Independent Networks in CD8(+) T Cells. Immunity *45*, 685–700. https://doi.org/10.1016/j.immuni.2016.07.022.
14. Baker, P.E., Gillis, S., Ferm, M.M., and Smith, K.A. (1978). The effect of T cell growth factor on the generation of cytolytic T cells. J. Immunol. *121*, 2168–2173.
15. Pipkin, M.E., Sacks, J.A., Cruz-Guilloty, F., Lichtenheld, M.G., Bevan, M.J., and Rao, A. (2010). Interleukin-2 and inflammation induce distinct transcriptional programs that promote the differentiation of effector cytolytic T cells. Immunity *32*, 79–90. https://doi.org/10.1016/j.immuni.2009.11.012.
16. Argüello, R.J., Combes, A.J., Char, R., Gigan, J.P., Baaziz, A.I., Bousiquot, E., Camosseto, V., Samad, B., Tsui, J., Yan, P., et al. (2020). SCENITH: A Flow Cytometry-Based Method to Functionally Profile Energy Metabolism with Single-Cell Resolution. Cell Metab. *32*, 1063–1075.e7. https://doi.org/10.1016/j.cmet.2020.11.007.
17. Cornish, G.H., Sinclair, L.V., and Cantrell, D.A. (2006). Differential regulation of T-cell growth by IL-2 and IL-15. Blood *108*, 600–608. https://doi.org/10.1182/blood-2005-12-4827.
18. Ray, J.P., Staron, M.M., Shyer, J.A., Ho, P.C., Marshall, H.D., Gray, S.M., Laidlaw, B.J., Araki, K., Ahmed, R., Kaech, S.M., and Craft, J. (2015). The Interleukin-2-mTORc1 Kinase Axis Defines the Signaling, Differentiation, and Metabolism of T Helper 1 and Follicular B Helper T Cells. Immunity *43*, 690–702. https://doi.org/10.1016/j.immuni.2015.08.017.
19. Pepper, M., Pagán, A.J., Igyártó, B.Z., Taylor, J.J., and Jenkins, M.K. (2011). Opposing signals from the Bcl6 transcription factor and the interleukin-2 receptor generate T helper 1 central and effector memory cells. Immunity *35*, 583–595. https://doi.org/10.1016/j.immuni.2011.09.009.
20. Xu, K., Yin, N., Peng, M., Stamatiades, E.G., Shyu, A., Li, P., Zhang, X., Do, M.H., Wang, Z., Capistrano, K.J., et al. (2021). Glycolysis fuels phosphoinositide 3-kinase signaling to bolster T cell immunity. Science (New York, N.Y.) *371*, 405–410. https://doi.org/10.1126/science.abb2683.
21. Feng, Q., Liu, Z., Yu, X., Huang, T., Chen, J., Wang, J., Wilhelm, J., Li, S., Song, J., Li, W., et al. (2022). Lactate increases stemness of CD8 + T cells to augment anti-tumor immunity. Nat. Commun. *13*, 4981. https://doi.org/10.1038/s41467-022-32521-8.
22. Wenes, M., Jaccard, A., Wyss, T., Maldonado-Pérez, N., Teoh, S.T., Lepez, A., Renaud, F., Franco, F., Waridel, P., Yacoub Maroun, C., et al. (2022). The mitochondrial pyruvate carrier regulates memory T cell differentiation and antitumor function. Cell Metab. *34*, 731–746.e9. https://doi.org/10.1016/j.cmet.2022.03.013.
23. Gismondi, A., Cifaldi, L., Mazza, C., Giliani, S., Parolini, S., Morrone, S., Jacobelli, J., Bandiera, E., Notarangelo, L., and Santoni, A. (2004). Impaired natural and CD16-mediated NK cell cytotoxicity in patients with WAS and XLT: ability of IL-2 to correct NK cell functional defect. Blood *104*, 436–443. https://doi.org/10.1182/blood-2003-07-2621.
24. Orange, J.S., Roy-Ghanta, S., Mace, E.M., Maru, S., Rak, G.D., Sanborn, K.B., Fasth, A., Saltzman, R., Paisley, A., Monaco-Shawver, L., et al. (2011). IL-2 induces a WAVE2-dependent pathway for actin reorganization that enables WASp-independent human NK cell function. J. Clin. Invest. *121*, 1535–1548. https://doi.org/10.1172/jci44862.
25. Hukelmann, J.L., Anderson, K.E., Sinclair, L.V., Grzes, K.M., Murillo, A.B., Hawkins, P.T., Stephens, L.R., Lamond, A.I., and Cantrell, D.A. (2016). The cytotoxic T cell proteome and its shaping by the kinase mTOR. Nat. Immunol. *17*, 104–112. https://doi.org/10.1038/ni.3314.
26. Oestreich, K.J., Read, K.A., Gilbertson, S.E., Hough, K.P., McDonald, P.W., Krishnamoorthy, V., and Weinmann, A.S. (2014). Bcl-6 directly represses the gene program of the glycolysis pathway. Nat. Immunol. *15*, 957–964. https://doi.org/10.1038/ni.2985.
27. van der Windt, G.J.W., Everts, B., Chang, C.H., Curtis, J.D., Freitas, T.C., Amiel, E., Pearce, E.J., and Pearce, E.L. (2012). Mitochondrial respiratory capacity is a critical regulator of CD8+ T cell memory development. Immunity *36*, 68–78. https://doi.org/10.1016/j.immuni.2011.12.007.
28. Man, K., and Kallies, A. (2015). Synchronizing transcriptional control of T cell metabolism and function. Nat. Rev. Immunol. *15*, 574–584. https://doi.org/10.1038/nri3874.
29. Cham, C.M., Driessens, G., O'Keefe, J.P., and Gajewski, T.F. (2008). Glucose deprivation inhibits multiple key gene expression events and effector functions in CD8+ T cells. Eur. J. Immunol. *38*, 2438–2450. https://doi.org/10.1002/eji.200838289.
30. Renner, K., Geiselhöringer, A.L., Fante, M., Bruss, C., Färber, S., Schönhammer, G., Peter, K., Singer, K., Andreesen, R., Hoffmann, P., et al. (2015). Metabolic plasticity of human T cells: Preserved cytokine production under glucose deprivation or mitochondrial restriction, but 2-deoxy-glucose affects effector functions. Eur. J. Immunol. *45*, 2504–2516. https://doi.org/10.1002/eji.201545473.

31. Kishore, M., Cheung, K.C.P., Fu, H., Bonacina, F., Wang, G., Coe, D., Ward, E.J., Colamatteo, A., Jangani, M., Baragetti, A., et al. (2017). Regulatory T Cell Migration Is Dependent on Glucokinase-Mediated Glycolysis. Immunity *47*, 875–889.e10. https://doi.org/10.1016/j.immuni.2017.10.017.

32. Amitrano, A.M., Berry, B.J., Lim, K., Kim, K.D., Waugh, R.E., Wojtovich, A.P., and Kim, M. (2021). Optical Control of CD8(+) T Cell Metabolism and Effector Functions. Front. Immunol. *12*, 666231. https://doi.org/10.3389/fimmu.2021.666231.

33. Garde, A., Kenny, I.W., Kelley, L.C., Chi, Q., Mutlu, A.S., Wang, M.C., and Sherwood, D.R. (2022). Localized glucose import, glycolytic processing, and mitochondria generate a focused ATP burst to power basement-membrane invasion. Dev. Cell *57*, 732–749.e7. https://doi.org/10.1016/j.devcel.2022.02.019.

34. Kelley, L.C., Chi, Q., Cáceres, R., Hastie, E., Schindler, A.J., Jiang, Y., Matus, D.Q., Plastino, J., and Sherwood, D.R. (2019). Adaptive F-Actin Polymerization and Localized ATP Production Drive Basement Membrane Invasion in the Absence of MMPs. Dev. Cell *48*, 313–328.e8. https://doi.org/10.1016/j.devcel.2018.12.018.

35. Brigida, I., Zoccolillo, M., Cicalese, M.P., Pfajfer, L., Barzaghi, F., Scala, S., Oleaga-Quintas, C., Álvarez-Álvarez, J.A., Sereni, L., Giannelli, S., et al. (2018). T cell defects in patients with ARPC1B germline mutations account for combined immunodeficiency. Blood *132*, 2362–2374. https://doi.org/10.1182/blood-2018-07-863431.

36. Castro, C.N., Rosenzwajg, M., Carapito, R., Shahrooei, M., Konantz, M., Khan, A., Miao, Z., Groß, M., Tranchant, T., Radosavljevic, M., et al. (2020). NCKAP1L defects lead to a novel syndrome combining immunodeficiency, lymphoproliferation, and hyperinflammation. J. Exp. Med. *217*, e20192275. https://doi.org/10.1084/jem.20192275.

37. Cook, S.A., Comrie, W.A., Poli, M.C., Similuk, M., Oler, A.J., Faruqi, A.J., Kuhns, D.B., Yang, S., Vargas-Hernández, A., Carisey, A.F., et al. (2020). HEM1 deficiency disrupts mTORC2 and F-actin control in inherited immunodysregulatory disease. Science (New York, N.Y.) *369*, 202–207. https://doi.org/10.1126/science.aay5663.

38. Lafouresse, F., Cotta-de-Almeida, V., Malet-Engra, G., Galy, A., Valitutti, S., and Dupré, L. (2012). Wiskott-Aldrich syndrome protein controls antigen-presenting cell-driven CD4+ T-cell motility by regulating adhesion to intercellular adhesion molecule-1. Immunology *137*, 183–196. https://doi.org/10.1111/j.1365-2567.2012.03620.x.

39. Salzer, E., Zoghi, S., Kiss, M.G., Kage, F., Rashkova, C., Stahnke, S., Haimel, M., Platzer, R., Caldera, M., Ardy, R.C., et al. (2020). The cytoskeletal regulator HEM1 governs B cell development and prevents autoimmunity. Sci. Immunol. *5*, eabc3979. https://doi.org/10.1126/sciimmunol.abc3979.

40. Nolz, J.C., Gomez, T.S., Zhu, P., Li, S., Medeiros, R.B., Shimizu, Y., Burkhardt, J.K., Freedman, B.D., and Billadeau, D.D. (2006). The WAVE2 complex regulates actin cytoskeletal reorganization and CRAC-mediated calcium entry during T cell activation. Curr. Biol. *16*, 24–34. https://doi.org/10.1016/j.cub.2005.11.036.

41. Pauker, M.H., Reicher, B., Joseph, N., Wortzel, I., Jakubowicz, S., Noy, E., Perl, O., and Barda-Saad, M. (2014). WASp family verprolin-homologous protein-2 (WAVE2) and Wiskott-Aldrich syndrome protein (WASp) engage in distinct downstream signaling interactions at the T cell antigen receptor site. J. Biol. Chem. *289*, 34503–34519. https://doi.org/10.1074/jbc.M114.591685.

42. Sims, T.N., Soos, T.J., Xenias, H.S., Dubin-Thaler, B., Hofman, J.M., Waite, J.C., Cameron, T.O., Thomas, V.K., Varma, R., Wiggins, C.H., et al. (2007). Opposing effects of PKCtheta and WASp on symmetry breaking and relocation of the immunological synapse. Cell *129*, 773–785. https://doi.org/10.1016/j.cell.2007.03.037.

43. Tamzalit, F., Wang, M.S., Jin, W., Tello-Lafoz, M., Boyko, V., Heddleston, J.M., Black, C.T., Kam, L.C., and Huse, M. (2019). Interfacial actin protrusions mechanically enhance killing by cytotoxic T cells. Sci. Immunol. *4*, eaav5445. https://doi.org/10.1126/sciimmunol.aav5445.

44. Bogucka-Janczi, K., Harms, G., Coissieux, M.M., Bentires-Alj, M., Thiede, B., and Rajalingam, K. (2023). ERK3/MAPK6 dictates CDC42/RAC1 activity and ARP2/3-dependent actin polymerization. Elife *12*, e85167. https://doi.org/10.7554/eLife.85167.

45. DeWane, G., Salvi, A.M., and DeMali, K.A. (2021). Fueling the cytoskeleton - links between cell metabolism and actin remodeling. J. Cell Sci. *134*, jcs248385. https://doi.org/10.1242/jcs.248385.

46. Holland, S.M., and Gallo, G. (2023). Actin cytoskeletal dynamics do not impose an energy drain on growth cone bioenergetics. J. Cell Sci. *136*, jcs261356. https://doi.org/10.1242/jcs.261356.

47. McQuin, C., Goodman, A., Chernyshev, V., Kamentsky, L., Cimini, B.A., Karhohs, K.W., Doan, M., Ding, L., Rafelski, S.M., Thirstrup, D., et al. (2018). CellProfiler 3.0: Next-generation image processing for biology. PLoS Biol. *16*, e2005970. https://doi.org/10.1371/journal.pbio.2005970.

48. Caldera, M., Müller, F., Kaltenbrunner, I., Licciardello, M.P., Lardeau, C.H., Kubicek, S., and Menche, J. (2019). Mapping the perturbome network of cellular perturbations. Nat. Commun. *10*, 5140. https://doi.org/10.1038/s41467-019-13058-9.

49. Vasconcelos, Z., Müller, S., Guipouy, D., Yu, W., Christophe, C., Gadat, S., Valitutti, S., and Dupré, L. (2015). Individual Human Cytotoxic T Lymphocytes Exhibit Intraclonal Heterogeneity during Sustained Killing. Cell Rep. *11*, 1474–1485. https://doi.org/10.1016/j.celrep.2015.05.002.

50. Picelli, S. (2019). Full-Length Single-Cell RNA Sequencing with Smart-seq2. Methods Mol. Biol. *1979*, 25–44. https://doi.org/10.1007/978-1-4939-9240-9_3.

51. Okonechnikov, K., Conesa, A., and García-Alcalde, F. (2016). Qualimap 2: advanced multi-sample quality control for high-throughput sequencing data. Bioinformatics *32*, 292–294. https://doi.org/10.1093/bioinformatics/btv566.

52. Dobin, A., Davis, C.A., Schlesinger, F., Drenkow, J., Zaleski, C., Jha, S., Batut, P., Chaisson, M., and Gingeras, T.R. (2013). STAR: ultrafast universal RNA-seq aligner. Bioinformatics *29*, 15–21. https://doi.org/10.1093/bioinformatics/bts635.

53. Liao, Y., Smyth, G.K., and Shi, W. (2019). The R package Rsubread is easier, faster, cheaper and better for alignment and quantification of RNA sequencing reads. Nucleic Acids Res. *47*, e47. https://doi.org/10.1093/nar/gkz114.

54. Love, M.I., Huber, W., and Anders, S. (2014). Moderated estimation of fold change and dispersion for RNA-seq data with DESeq2. Genome Biol. *15*, 550. https://doi.org/10.1186/s13059-014-0550-8.

55. Dupré, L., Boztug, K., and Pfajfer, L. (2021). Actin Dynamics at the T Cell Synapse as Revealed by Immune-Related Actinopathies. Front. Cell Dev. Biol. *9*, 665519. https://doi.org/10.3389/fcell.2021.665519.

56. Dupré, L., Houmadi, R., Tang, C., and Rey-Barroso, J. (2015). T Lymphocyte Migration: An Action Movie Starring the Actin and Associated Actors. Front. Immunol. *6*, 586. https://doi.org/10.3389/fimmu.2015.00586.

57. Pollard, T.D. (2016). Actin and Actin-Binding Proteins. Cold Spring Harb. Perspect. Biol. *8*, a018226. https://doi.org/10.1101/cshperspect.a018226.

58. Foroutan, M., Bhuva, D.D., Lyu, R., Horan, K., Cursons, J., and Davis, M.J. (2018). Single sample scoring of molecular phenotypes. BMC Bioinf. *19*, 404. https://doi.org/10.1186/s12859-018-2435-4.

STAR★METHODS

KEY RESOURCES TABLE

REAGENT or RESOURCE	SOURCE	IDENTIFIER
Antibodies		
Anti-CD3 (clone SK7) APC	Becton Dickinson	Cat# 345767; RRID: AB_2833003
Anti-CD4 (clone RPA-T4) PerCP-Cy5.5	Becton Dickinson	Cat# 560650; RRID: AB_1727476
Anti-CD8 (clone RPA-T8) V450	Becton Dickinson	Cat# 560347; RRID: AB_1645581
Anti-CD8 PerCP Cy5.5 (clone MEM-31)	Sysmex	Cat# AE134275
Anti-CD18/LFA-1 β2 subunit (clone 6.7) PE-Cy5	Becton Dickinson	Cat# 557528; RRID: AB_2296304
Anti-CD18/LFA-1 β2 subunit (clone m24) AF 647	Biolegend	Cat# 363412; RRID: AB_2716175
Anti-CD107a/LAMP-1 (cloneH4A3) PE	Biolegend	Cat# 328607; RRID: AB_1186062
Anti-granzyme B (clone GB11) PE	eBioscience	Cat# 12-8899-41; RRID: AB_1659718
Anti-perforin (clone dG9) AF488	BioLegend	Cat# 308108; RRID: AB_493252
Anti-CD3 (Clone OKT3)	eBioscience	Cat# 16-0037-85; RRID:AB_468854
Anti-ARPC1B (polyclonal rabbit)	Sigma Aldrich	Cat# HPA004832; RRID: AB_1845044
Anti-HEM1/NCKAP1L (polyclonal rabbit)	Sigma Aldrich	Cat# HPA039490
Anti-WASP (clone B-9)	Santa Cruz Biotechnology	Cat# sc-13139; RRID: AB_628445
Anti-HSP90 (clone F-8)	Santa Cruz Biotechnology	Cat# sc-13119; RRID:AB_675659
Anti-GAPDH (clone 6C5)	Santa Cruz Biotechnology	Cat# sc-32233; RRID: AB_627679
Anti-β-actin (clone AC-15)	Thermofisher scientific	Cat# AM4302; RRID: AB_2536382
Anti-mouse IgG, HRP-linked antibody	Cell Signaling	Cat# 7076S; RRID: AB_330924
Anti-CD8 (clone RPA-T8) APC	Becton Dickinson	Cat# 555369; RRID: AB_398595
Anti-puromycin (clone 12D10) Alexa Fluor 647	Merck	Cat# MABE343
Biological samples		
Peripheral blood from healthy donors	Etablissement Français du Sang (EFS Occitanie)	N/A
Peripheral blood mononuclear cells from 3 ARPC1B-deficient patients, 3 WASP-deficient patients and 2 HEM-1-deficient patients	San Raffaele Hospital, Milan Italy; Saint Anna Children's Hopital, Vienna, Austria; Institut Universitaire du Cancer de Toulouse - Oncopole, Toulouse, France	See German et al.,[12] Salzer et al.[39]
Chemicals, peptides, and recombinant proteins		
2-deoxy-glucose	Abcam	F1009
Oligomycin A	Sigma-Aldrich	75351
Antimycin A	Sigma-Aldrich	A8674
Rotenone	Sigma-Aldrich	R8875
Carbonylcyanid-4-(trifluromethoxy) phenylhydrazone (FCCP)	Sigma-Aldrich	C2920
Shikonin	ABCR GmbH	AB141601
Galloflavin	Biotrend Chemikalien	AOB1024-1
3-bromopyruvate	Sigma-Aldrich	16490
Puromycin	Sigma-Aldrich	P7255
Alexa Fluor 488 phalloidin	Invitrogen	A12379
Alexa Fluor 546 phalloidin	Invitrogen	A22283
DAPI	Invitrogen	D1306
Cell Trace Violet	Invitrogen	C34571 A
Viability dye	eBioscience	65-0865-14
Recombinant human ICAM-1 Fc chimera protein	R&D Systems	720-IC-200

(*Continued on next page*)

Continued

REAGENT or RESOURCE	SOURCE	IDENTIFIER
RPMI 1640 Medium	Gibco	21875034
IL-2	Peprotech	200–02
IL-7	Peprotech	200–07
IL-15	Peprotech	200–15
Recombinant human CXCL12	Peprotech	300-28A
HEPES	Gibco	15630–056
Poly-L-lysine solution	Sigma-Aldrich	P4832
100x MEM non-essential amino acids	Gibco	M-7145
Sodium pyruvate	Gibco	11360–039
Penicillin-streptomycin	Gibco	15140–122
Heat-inactivated human serum	Sigma-Aldrich	H5667
Heat-inactivated fetal bovine serum	Sigma-Aldrich	F7552
Human $CD8^+$ T cell positive selection kit	Thermofisher scientific	8802-6832-74
Human $CD8^+$ T cell enrichment kit	Thermofisher scientific	8804-6812-74
Dimethyl Sulfoxide	Sigma-Aldrich	D8418
Lectin from *Phaseolus vulgaris*	Sigma-Aldrich	L1668
Critical commercial assays		
CellTiter-Glo luminescent cell viability assay	Promega	G7570
G-Actin: F-Actin *in vivo* assay kit	Cytoskeleton Inc	BK037
Deposited data		
High content cell imaging codes	This paper	Zenodo Data: https://doi.org/10.5281/zenodo.10490293
Bulk RNA-Seq dataset	This paper	Dryad Data: https://doi.org/10.5061/dryad.69p8cz98t
Experimental models: Cell lines		
P815 mastocytoma cell line of murine origin (DBA/2 strain)	ATCC	TIB-64
Software and algorithms		
FlowJo	Treestar	V10.3
ImageJ	National Institutes of Health	V1.54g
CellProfiler	Broad Institute	V4.2.6
Harmony	Perkin Elmer	V4.9
RStudio	Cran, The R foundation	https://www.r-project.org
Prism 8	GraphPad	V8.3
Python	National Institutes of Health	N/A

RESOURCE AVAILABILITY

Lead contact

Further information and requests for resources and reagents should be directed to and will be fulfilled by the lead contact, Loïc Dupré, Department of Dermatology, Medical University of Vienna, Währinger Gürtel 18–20, 1090 Vienna, Austria. (loic.dupre@meduniwien.ac.at)

Materials availability

This study did not generate new unique reagents.

Data and code availability

- Data presented in the paper including image datasets, morphological measurements, Western blots, flow cytometry and luminescence data are available from the lead contact upon request.
- The original code used to extract morphological measurements from the confocal images has been deposited at Zenodo and is publicly available as of the date of publication. The corresponding DOI is listed in the key resources table.

- RNA-seq data have been uploaded to the DRYAD data repository. The corresponding DOI is listed in the key resources table.
- Any additional information required to reanalyze the data reported in this paper is available from the lead contact upon request.

EXPERIMENTAL MODEL AND STUDY PARTICIPANT DETAILS

Patients

Information pertaining to patients who have been reported in previous studies is summarized in Figure S9C. Beyond the mutational status reported in Figure S9C for all considered patients, the description of unpublished patients is as follows: ARPC1B deficient patient 2 (Pt2) is a male patient with a disease onset at 2 months. He presented with oral moniliasis, severe malnutrition, cleft palate, leukocytosis, failure to thrive (3 kg/51 cm) and developmental delay. Laboratory findings pointed to low neutrophil oxidative burst (DHR assay).

Library of patient-derived CD8$^+$ T cells

Patient CD8$^+$ T lymphocytes were extracted from frozen PBMCs of fourteen healthy donors, three ARPC1B-, two HEM1-, and three WASP-deficient patients (see "patients" section above) via MagniSort Human CD8$^+$ T cell Enrichment Kit (ThermoFisher). CD8$^+$ T cells were kept in RPMI-based growth media (RPMI media (Gibco), 5% human serum (heat inactivated, AB positive blood type, Institut de Biotechnologies Jacques Boy, France), 100 U/mL penicillin/streptomycin (Gibco), 1 mM sodium pyruvate (Gibco), 1X MEM non-essential amino acids (Sigma), 10 mM HEPES (Gibco). For expansion CD8$^+$ T cells were stimulated with 2 μg/mL phytohemagglutinin (PHA-P, Sigma) and a mixture of irradiated PBMCs from three healthy donors and kept in RPMI-based growth media supplemented with 100 U/mL IL-2. At day 10 post-stimulation, samples of cultured cells were controlled for absence of mycoplasma contamination, purity of CD8$^+$ T cells, expression of phenotypic markers and western-blot analysis of specific protein deficiency. Cultures contaminated with mycoplasma were discarded. T cell cultures with more than 10% of CD4$^+$ T cells were subjected to a second round of CD8$^+$ T cell purification and expansion. Controlled CD8$^+$ T cell cultures were harvested at day 10 post-stimulation and frozen in fetal calf serum (FCS, Sigma) supplemented with 10% DMSO (Sigma). Peripheral blood from healthy donors and patients was obtained in accordance with the 1964 Helsinki declaration and its later amendments or ethical standards. Informed consents were approved by the relevant local Institutional Ethical Committees.

METHOD DETAILS

Phenotypic characterization of the effector CD8$^+$ T cells

Expanded CD8$^+$ T cells were stained with fluorochrome-conjugated Ab recognizing the extracellular markers CD3, CD4, CD8, CD18 and CXCR4 (all from BD-Pharmingen) for 30 min on ice. Staining of intracellular proteins was performed after fixation with 1% PFA and permeabilization with Ab specific for perforin (BioLegend) and granzyme B (eBioscience). Stained cells were further analyzed first with fluorescent flow cytometer (Fortessa, BD). Flow cytometry data was processed using FlowJo Software.

Analysis of protein expression

For analysis of protein expression $\sim 10^6$ T cells were harvested. Cells were rinsed in PBS and resuspended in lysis buffer (RIPA (Millipore), protease/phosphatase inhibitors (ThermoFisher Scientific)), incubated 20 min on ice and cleared by centrifugation. Cleared lysates were mixed with Laemmli sample buffer (BioRad), boiled and subjected to SDS-PAGE. Following separation proteins were transferred to nitrocellulose membranes (GE Healthcare) and visualized with anti-ARPC1B (Sigma; HPA004832), WASP (Santa Cruz Biotechnology B-9) or HEM1 (Sigma; HPA039490) Ab followed by incubation with secondary HRP-conjugated Ab (Cell Signaling). Protein loading control was done by staining GAPDH or HSP90 with corresponding Abs (both from Santa Cruz Biotechnology). Stained membranes were incubated with Super Signal West Pico Chemiluminescence Substrate (ThermoFisher Scientific) and read with 16-bit digital camera (Bio-Rad).

High-content stimulation and staining of T cells

384-well plates (CellCarrier-384 Ultra, PerkinElmer) were functionalized O/N at 4°C with either 4 μg/mL recombinant human ICAM-1-Fc chimera (R&D Systems) or a combination of 2 μg/mL recombinant human ICAM-1-Fc chimera (R&D Systems) and 10 μg/mL anti-CD3 Ab (OKT3, eBioscience). Next day, wells were washed with 50 μL of T cell RPMI-based growth media. Frozen CD8$^+$ T cells were thawed with warm T cell RPMI-based growth media, split to 2 equal portions and incubated in growth media with or without 100 U/mL IL-2 overnight. On the day of experiment, a small aliquot of each sample was taken for bulk RNA-seq. Prepared cells were next seeded to pre-coated and washed 384-multiwell plates at 10′000 cells per well, gently pushed down by low-speed (70 rcf) centrifugation for 10 s and incubated for 15 min at 37°C in cell culture incubator. Following stimulation cells were fixed with 4% paraformaldehyde and stained with anti-CD8 APC-conjugated Ab (BD Pharmingen) and phalloidin-AF488 (ThermoFisher) in permeabilization buffer (eBioscience). Nuclei were stained with DAPI (Sigma). Stained cells were rinsed once with 50 μL of PBS and stored at 4°C in the dark until imaging. To account for possible well-to-well variability and plate effect, each cell group was seeded in 2 groups of 4 wells at least half a plate apart (8 single-well replicas in total).

High-content image acquisition and processing

Stained 384-multiwell plates were equilibrated to room temperature and recorded with a high-content screening system (Opera Phenix, PerkinElmer) equipped with a 40×1.1 NA Plan Apochromat water immersion objective, sCMOS cameras (16 bits, 6.5 μm pixel) and Yokogawa spinning disk confocal unit. For each well we acquired 9 fields-of-view and 4 Z-planes per field (with step of 0.5 μm, starting at the cell contact plane with the substrate). Z-stacks of images were projected along z axis using maximum intensity projection using ImageJ. Z-projected data was then processed with CellProfiler V4.2.6.[47] First, nuclei were located via DAPI staining using global minimum cross entropy thresholding. Following nuclei detection, a secondary object – outline of the cells was identified via watershed method and thresholding on the phalloidin-AF488. Following segmentation of nuclei and cell outlines, various morphological parameters were extracted targeting changes in shape of nuclei and cells, intensity and texture of DAPI and phalloidin using CellProfiler library of measurements. Final dataset comprised of a total of 3121 morphological features per detected object. Next dead cells and debris were identified in the dataset using machine learning (Random Forest algorithm, scikit-learn, Python) trained on 30% of manually annotated dataset representing random 1000 objects from the entire dataset. The $CD8^+$ T cell population was then extracted using manually set gates on total intensity of CD8 within each object. For each donor we next resampled the dataset (without replacement) using 40 random cells per sample and recorded average value for each morphological feature per sample. Resampled dataset of $CD8^+$ T cells was used to extract robust and informative features using combination of standard scoring and network-based filtering.[48] On average 150–170 morphological features remained after filtration.

T cell morphology, adhesion, and motility upon treatment with glycolysis and OXPHOS inhibitors

Primary human $CD8^+$ T cells previously grown in complete medium with 100 U/mL IL-2 were treated with either 50 mM 2-deoxy-D-glucose (2-DG, Sigma Aldrich) or 1 μM oligomycin A (Sigma Aldrich). Cells were immediately seeded into eight-well μ-slides (Ibidi) precoated with 4 μg/mL recombinant human ICAM-1-Fc chimera (R&D Systems). Following incubation for 3 h at 37°C 5% CO_2, cells were fixed with 3% PFA and stained overnight with Alexa Fluor 546 conjugated phalloidin (Invitrogen) in permeabilization buffer (eBioscience). The nucleus was stained with DAPI for 1 min at room temperature. The slides were stored in PBS until image acquisition with a Zeiss LSM 710 confocal microscope equipped with a 40× oil objective. Analysis of F-actin intensities as well as morphological features was performed with the Fiji ImageJ software on a minimum of 100 cells per condition and experiment. Alternatively, $CD8^+$ T cells were treated for 2 h with the above indicated 2-DG and oligomycin concentrations and seeded in 384-well plates (CellCarrier-384 Ultra, PerkinElmer) previously functionalized with 2 μg/mL recombinant human ICAM-1-Fc chimera (R&D Systems) and 10 μg/mL anti-CD3 Ab (OKT3, eBioscience). After 20 min, plates were flipped in order to discard non-adherent cells. Remaining cells were fixed with 3% paraformaldehyde for 10 min at 37°C and permeabilized with permeabilization buffer (eBioscience). Cells were stained with Alexa Fluor 546 phalloidin (Invitrogen) overnight, and with DAPI for 5 min. Plates were stored in PBS until acquisition with a high-content screening system (Opera Phenix, PerkinElmer) equipped with a 40×1.1 NA Plan Apochromat water immersion objective sCMOS cameras (16 bits, 6.5 μm pixel) and Yokogawa spinning disk confocal unit. Images were analyzed with Harmony software (PerkinElmer) in order to extract the number of adherent cells per well, as well as the F-actin intensity and area of those cells. The proportion of adherent cells was calculated by comparing the number of detected cells in the various experimental wells to that in control wells not subjected to washing steps. For assessment of motility, $CD8^+$ T cells were prestained with CTV and then treated with 2-DG or oligomycin for 2 h. For confined migration assessment, cells were loaded into an under-agarose setup consisting in a coating of 2 μg/mL recombinant human ICAM-1-Fc chimera (R&D Systems) a thin layer of 0.5% agarose and 2 holes for the loading of 100 ng/mL CXCL12 (Peprotech) in one and the cells (1×10^4) in the other. For chemotaxis assessment, Ibidi chemotaxis μ-slides were coated with 1 μg/mL ICAM-1. The chemokine gradient was created by loading the two-side chambers with RPMI based medium and adding CXCL12 (Peprotech) at a final concentration of 100 ng/mL in one of the chambers. $CD8^+$ T cells pre-stimulated with IL-2, IL-7 and IL-15 were pre-stained with CellTracker Green CMFDA (Invitrogen) and then treated with 2-DG or oligomycin. Around 100,000 cells were then loaded on the middle channels of the Ibidi slides. The slides were incubated for 1 h at 37°C 5% CO2. Cell migration was recorded on an Eclipse TE2000-E fully-motorized inverted microscope (Nikon) and a 10x/0.45 NA objective. The microscope was equipped with an incubation chamber for temperature and CO2 control. Images were acquired using sCMOS camera (Hamamatsu) and Metamorph software (Molecular Devices), for 16 h at a rate of 1 image every 2 min. The TrackMate tool on ImageJ was used for image processing and extraction of cell motility parameters.

Metabolic status with the SCENITH assay

$CD8^+$ T cells from three healthy donors were used to perform the SCENITH assay.[16] Experimental duplicates were performed in each condition. Cells were seeded in a 96-well plate and were treated for 10–15 min with control, 2-DG (100 mM), oligomycin (1 μM), or sequentially with both the drugs. Cells were then treated with puromycin (10 μg/mL) for 45 min. After puromycin treatment, cells were washed with cold PBS and stained with Alexa Fluor 488-labelled phalloidin for 25 min at 4°C in FACS buffer. After washing, cells were fixed and permeabilized using FOXP3 fixation and permeabilization buffer. Intracellular staining of puromycin was done using Alexa Fluor 647-labelled anti-puromycin Ab. Fluorescence was measured using flow cytometry (Cytek Aurora) and analyzed with FlowJo software (FlowJo, Ashland, Ore).

Kinetics of cytotoxic activity

$CD8^+$ T cells from 14 healthy donors and 3 ARPC1B deficient patients were stimulated with or deprived of IL-2 overnight. GFP-expressing P815 target cells were coated with the indicated concentrations of anti-CD3 Ab (OKT3 clone, eBioscience) during 1 h at 37°C/5% CO_2. P815 target cells and $CD8^+$ T cells were transferred at a 2:1 ratio in the wells of a 384-well plate (PerkinElmer). Aphidicolin (Sigma) was added at 0.1 μg/mL to prevent target cell proliferation and allow net measurement of lymphocyte-mediated cytotoxicity.[49] Well content was recoded every 2 h for 24 h with an automated HCS device (Opera Phenix, PerkinElmer) equipped with temperature and CO_2 control. Cytotoxicity was analyzed by counting the number of alive target cells. Integrated killing was calculated by calculating the sum of percentage of dead target cells at every 2-h interval.

Assessment of degranulation by cytometry

GFP-expressing P815 target cells were coated with 1 μg/mL of anti-CD3 Ab (OKT3 clone, eBioscience). $CD8^+$ T cells were either left untreated or treated with 50 mM 2-DG or 1 μM oligomycin. P815 target cells were then co-cultured with pretreated T cells for 2 h at 37°C/5% CO_2 at a ratio of 1 target cell for 2 T cells. Anti-CD107a Ab was added from the outset of the co-culture, and anti-CD18/LFA-1 β2 subunit m24 Ab (Biolegend) and viability dye (eBioscience) were added to the wells 20 min before the end of the 2-h co-culture. The T cells were stained with an anti-CD8 Ab (Sysmex) for 20 min. Samples were acquired on Fortessa (BD Biosciences) and analyzed with FlowJo software (FlowJo, Ashland, Ore).

RNA sequencing and raw data processing

Five hundred cells were lysed in 4 μL of lysis buffer and cDNA synthesis and enrichment were performed following the Smart-seq2 protocol.[50] Briefly library preparation was conducted on 1 ng of cDNA using the Nextera XT library preparation kit (Illumina). Sequencing was performed using the 50 bp single-read setup on the Illumina HiSeq 3000/4000 platform. Illumina adaptors were trimmed from raw reads using Picard tools (GATK). Basic quality control of 50 bp single end reads was performed with fastQC. Additional, qualimap and fastqc-screen reports were screened for outlying samples in terms of multimapping reads, possible contaminations (rRNA, intronic RNA, *E. coli*, etc.) and distribution of read coverage.[51] Reads were then aligned to human genome build GRCh38 using STAR aligner with standard settings.[52] Aligned reads were counted using featureCounts function of Rsubread package.[53] The resulting count matrix was then analyzed using DESeq2 pipeline.[54]

Transcriptome analysis

Association tests were performed using a negative binomial model as implemented in DESeq2. To assess the overlap between gene lists obtained from regression analysis and curated gene sets such MSigDB Hallmark genes, Wiki Pathways Human, GO Biological process we calculated hypergeometric tests followed p value adjustment for multiple testing as implemented in R package clusterProfiler. Gene lists were curated based on literature pertaining to actin cytoskeleton[55–57] and metabolic pathways.[26] For selected gene lists we calculated scores using singscore method[58] and compared them to morphological features.

ATP content measurement with CellTiter-Glo assay

Cellular ATP production was assessed using CellTiter-Glo Luminescent Cell Viability Assay (Promega). For comparison of cells treated with or without IL-2, cells were thawed and plated with or without IL-2 (20 ng/mL) and incubated for 24 h at 37°C. To assess the effect of metabolic drugs on ATP production, 10,000 cells were plated in 25 μL of medium in each well of a 96 well flat bottom plate. 25 μL of drug solutions or medium was added to reach the final concentrations of 50 mM 2-DG, 10 μM 3-bromopyruvate (Sigma), 10 μM shikonin (ABCR), 10μM galloflavin (Biotrend) and OXPHOS inhibitors oligomycin, antimycin-A, FCCP, rotenone, each at 1 μM. Drugs were incubated for 2 h at 37°C and 30 min at room temperature. To compare ARPC1B patient cells with healthy controls, cells were thawed and plated with or without IL-2, 96 h before ATP measurement. 10,000 cells were plated in 50 μL per well in a 96 well flat-bottom plate and equilibrated to room temperature for 30 min. CellTiter-Glo reagent was equilibrated to room temperature and 50 μL of reagent added to each well. To lyse the cells, the plates were placed on a shaker for 2 min, then incubated for 10 min at room temperature. Luminescence was detected using a microplate reader (Hidex Sense).

Measurement of G-actin and F-actin contents in T cells

G-actin and F-actin contents were assessed using the G-actin/F-actin *In Vivo* Assay Kit (Cytoskeleton, Inc.). T cells were thawed and plated overnight at 37°C with or without 20 ng/mL IL-2. Initially, 1 × 10^7 cells were harvested through centrifugation and re-suspended in LAS2 actin stabilization buffer. The cell pellet was then homogenized, and lysates were incubated at 37°C. A 100 μL portion of each lysate was centrifuged to remove unbroken cells or tissue debris. The supernatants were then transferred to ultracentrifuge tubes and centrifuged again, separating F-actin and G-actin. Actin depolymerization buffer was added to the F-actin pellet. Finally, both pellet and supernatant samples were mixed with SDS sample buffer and quantitated through SDS-PAGE and western blot analysis. An anti-actin mouse monoclonal antibody was used to detect actin, followed by chemiluminescent detection. Western blots semi-quantification was performed using ImageJ software.

T cell morphology upon treatment with glycolytic inhibitors and OXPHOS inhibitors

384-well plates (CellCarrier-384 Ultra, PerkinElmer) were functionalized O/N at 4°C with either 4 μg/mL recombinant human ICAM-1-Fc chimera (R&D Systems) or a combination of 2 μg/mL recombinant human ICAM-1-Fc chimera (R&D Systems) and 10 μg/mL anti-CD3 Ab (OKT3, eBioscience). T cells from three healthy donors were thawed and incubated with IL-2 overnight. On the following day the cells were treated with 50 mM 2-DG, 10 μM 3-bromopyruvate, 10 μM shikonin, 10 μM galloflavin and OXPHOS inhibitors oligomycin, antimycin-A, FCCP, rotenone, each at 1 μM, for 2 h. Prepared cells were next seeded to pre-coated and washed 384-multiwell plates at 10,000 cells per well, gently pushed down by low-speed (100 rcf) centrifugation for 10 s and incubated for 15 min at 37°C in cell culture incubator. Following stimulation cells were fixed with 3% paraformaldehyde and stained with anti-CD8 APC-conjugated Ab (BD Pharmingen) and phalloidin-AF488 (ThermoFisher) in permeabilization buffer (eBioscience). Nuclei were stained with DAPI (Sigma). Stained cells were rinsed once with 50 μL of PBS and stored at 4°C in the dark until imaging.

QUANTIFICATION AND STATISTICAL ANALYSIS

All statistical analysis was performed using python, R and GraphPad Prism. Explanation of statistical analysis used to quantify data has been systematically described in all the figure legends. All the statistical parameters such as exact value of n, p value, Pearson's co-efficient (r) are described in the figure legends. When several conditions were to compare, we performed a one-way ANOVA, followed by Tukey range test to assess the significance among pairs of conditions. When only two conditions were to test, we performed paired t test.

Cell Reports, Volume *43*

Supplemental information

Coordinated ARP2/3 and glycolytic activities regulate the morphological and functional fitness of human CD8$^+$ T cells

Anton Kamnev, Tanvi Mehta, Matthias Wielscher, Beatriz Chaves, Claire Lacouture, Anna-Katharina Mautner, Lisa E. Shaw, Michael Caldera, Jörg Menche, Wolfgang P. Weninger, Matthias Farlik, Kaan Boztug, and Loïc Dupré

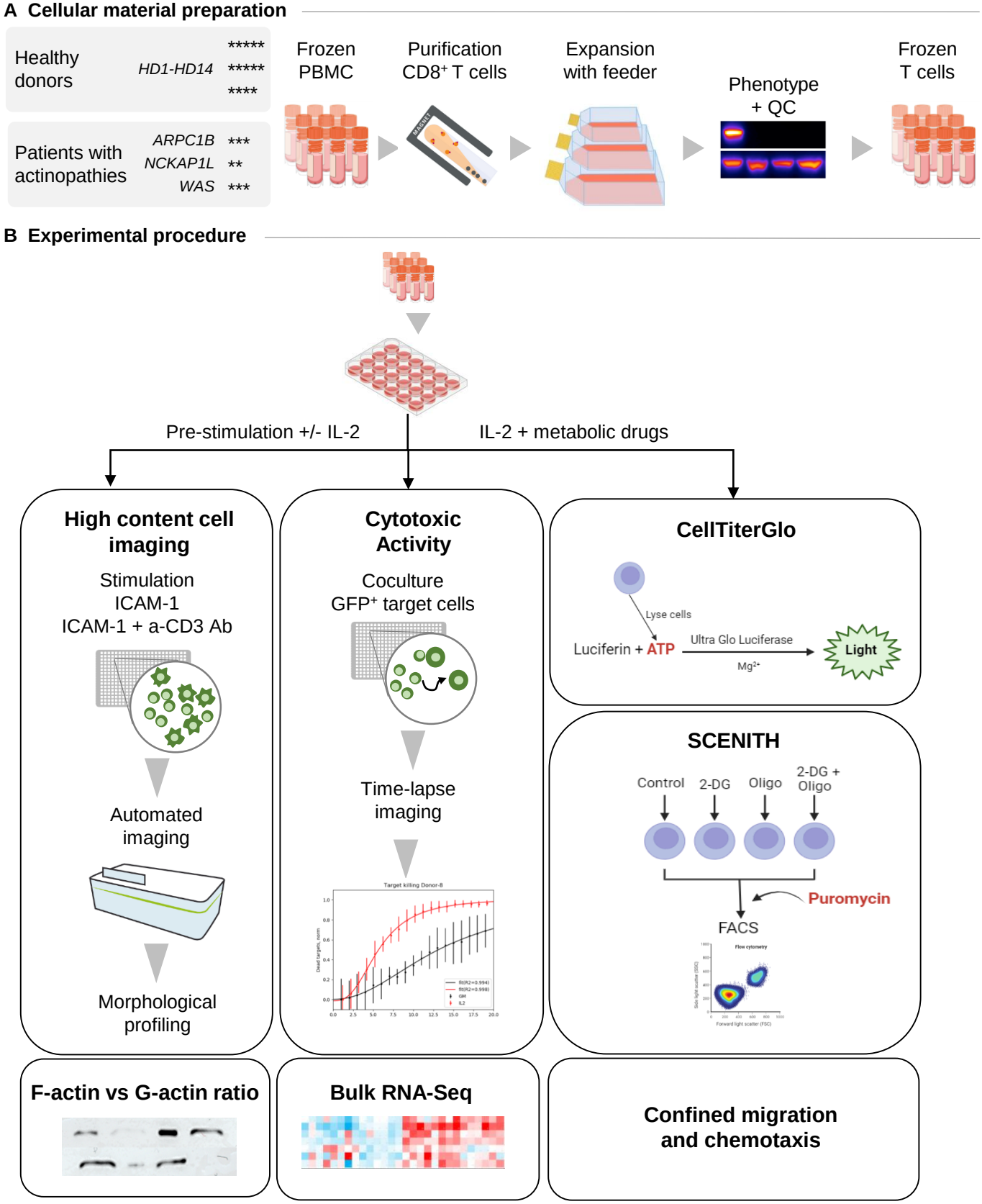

Figure S1. Experimental workflow
(A) Preparation of a CD8⁺ T cell library from PBMCs of healthy donors and patients with actinopathies.
(B) T cells were pretreated with IL-2 and tested in parallel for morphological fitness, cytotoxic activity and transcriptional activity and metabolic status.

A

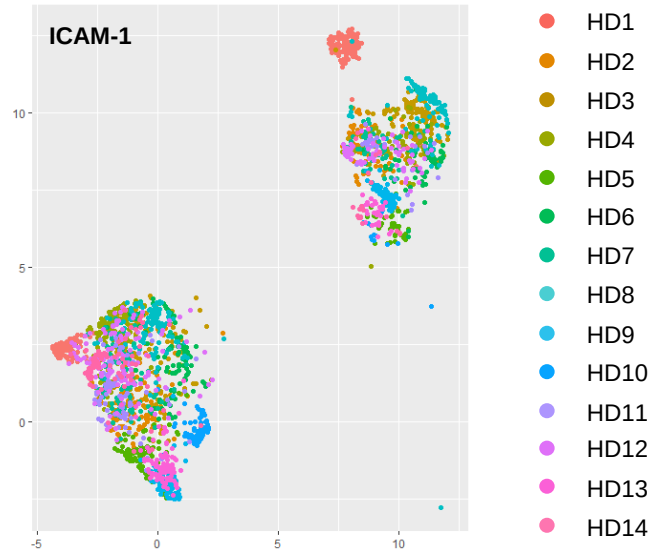

B

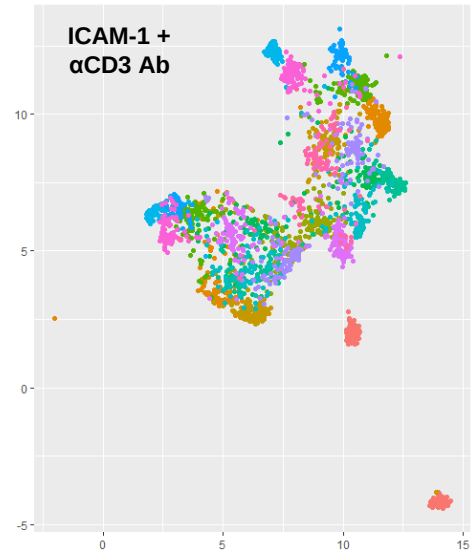

C **PCA loadings (ICAM-1)**

Feature	PC1	PC2
Cell area	0.97	0.08
EOCP	0.07	-0.92
Eccentricity	0.17	-0.43
F-actin density	0.03	-0.12
F-actin total	0.28	-0.65

D **PCA loadings (ICAM-1 + αCD3 Ab)**

Feature	PC1	PC2
Cell area	0.99	0.06
EOCP	0.08	-0.82
Eccentricity	0.59	-0.03
F-actin density	0.005	-0.02
F-actin total	0.02	-0.55

Figure S2. Change in T cell morphology following treatment with IL-2

(A) Morphological profiling of human $CD8^+$ T cells stimulated over ICAM-1 and treated or not with IL-2. UMAP plots correspond to the aggregation of 173 features extracted from automatically acquired confocal images. They highlight the distinct morphological profile of IL-2 treated cells on both stimuli. Each dot represents a pool of 20 individual cells. Data are derived from 14 healthy donors.

(B) Morphological profiling of human $CD8^+$ T cells stimulated over ICAM-1 and anti-CD3 ab and treated or not with IL-2. UMAP plots correspond to the aggregation of 173 features extracted from automatically acquired confocal images. They highlight the distinct morphological profile of IL-2 treated cells on both stimuli. Each dot represents a pool of 20 individual cells. Data are derived from 14 healthy donors.

(C) PCA loadings of average cell morphology for each donor stimulated with ICAM built using 5 key morphological parameters (averaged across all samples for each donor).

(D) PCA loadings of average cell morphology for each donor stimulated with ICAM + anti-CD3 Ab built using 5 key morphological parameters (averaged across all samples for each donor).

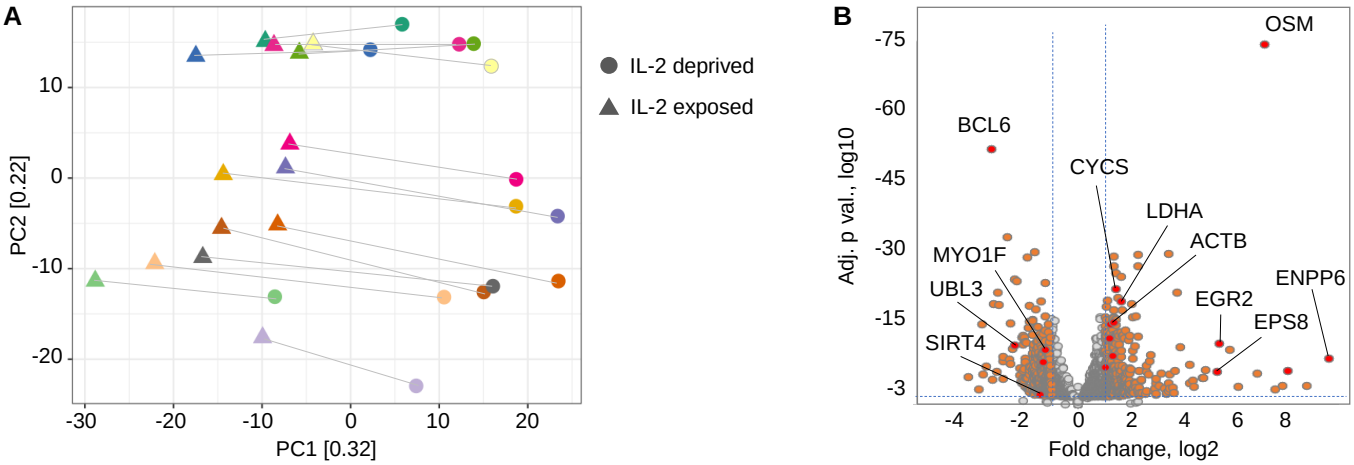

Figure S3. Transcriptional activity of IL-2 in effector CD8⁺ T cells

(A) PCA plot of gene expression data from healthy donor CD8+ T cells. Individual colours indicate donors. Grey lines connect data points from same donor for IL-2 deprived and exposed groups.

(B) Volcano plot highlighting significant changes in gene expression between IL-2 deprived and exposed healthy donor CD8+ T cells.

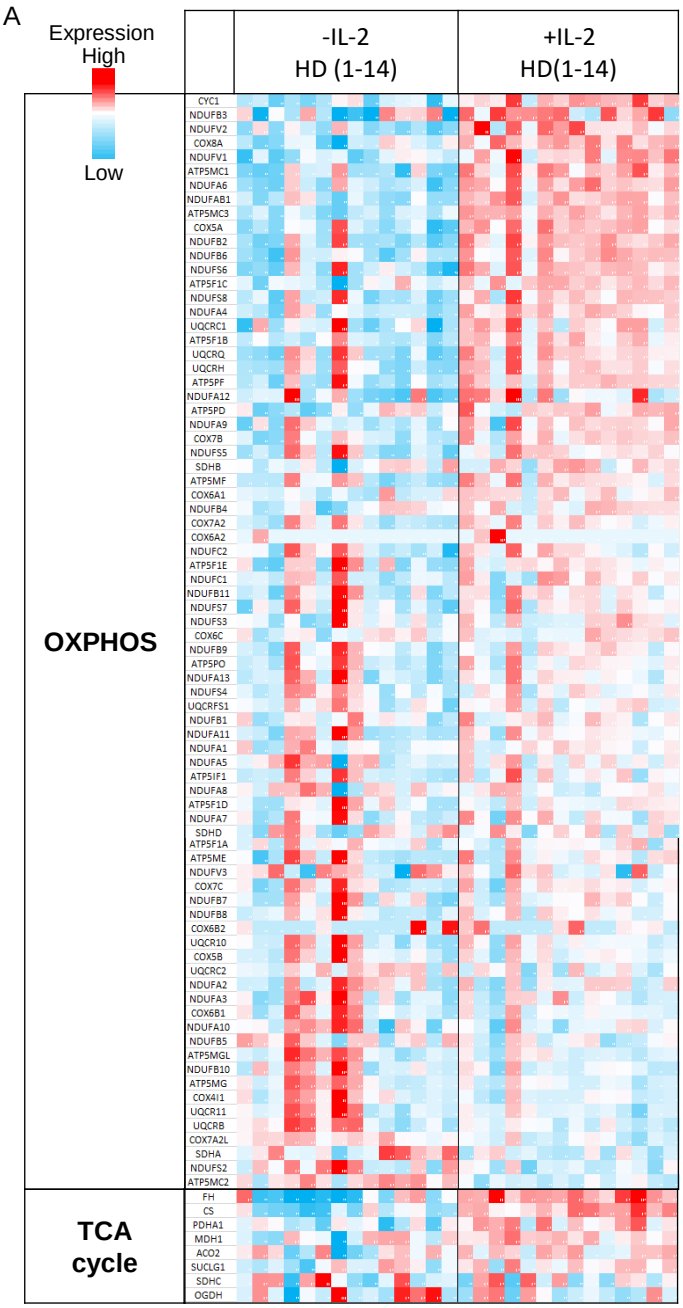

Figure S4. Expression of genes involved in OXPHOS and TCA cycle.
A) Heatmap of changes in expression of OXPHOS genes between IL-2 deprived and IL-2 exposed CD8⁺ T cells from 14 healthy donors.
(B) Heatmap of changes in expression of TCA cycle genes between IL-2 deprived and IL-2 exposed CD8⁺ T cells from 14 healthy donors.

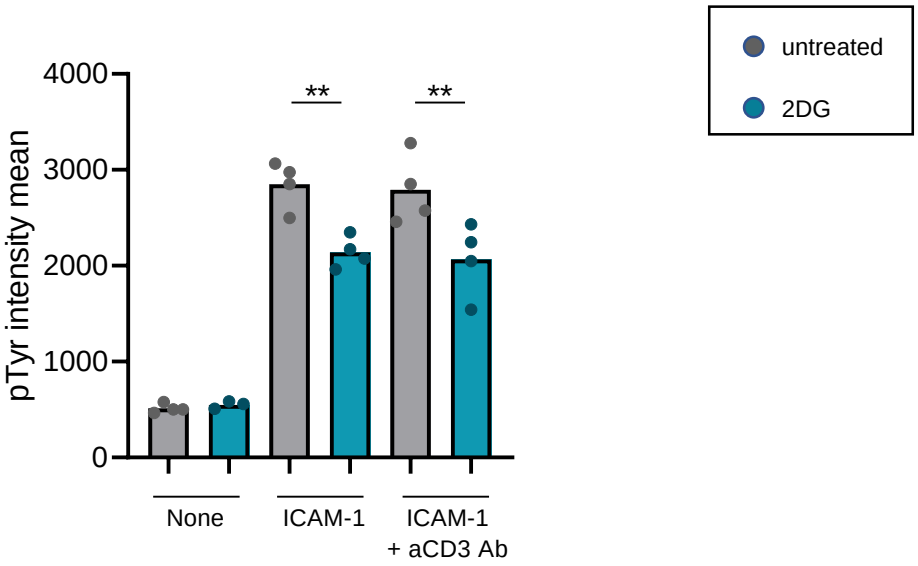

Figure S5. Change in pTyr intensity following treatment with 2DG.

Mean Phosphorilated Tyrosine (Y99) intensity at the adhesion plane of human $CD8^+$ T cells stimulated over ICAM-1/ICAM-1 + aCD3 Ab treated or not with 2-DG. Each dot represents a replicate from one representative individual experiment out of 2. One-way Anova Sidak's multiple comparisons test was used for statistical evaluation. ns = $p > 0.05$; * = $p \leq 0.05$; ** = $p \leq 0.01$; *** = $p \leq 0.001$; **** = $p \leq 0.0001$.

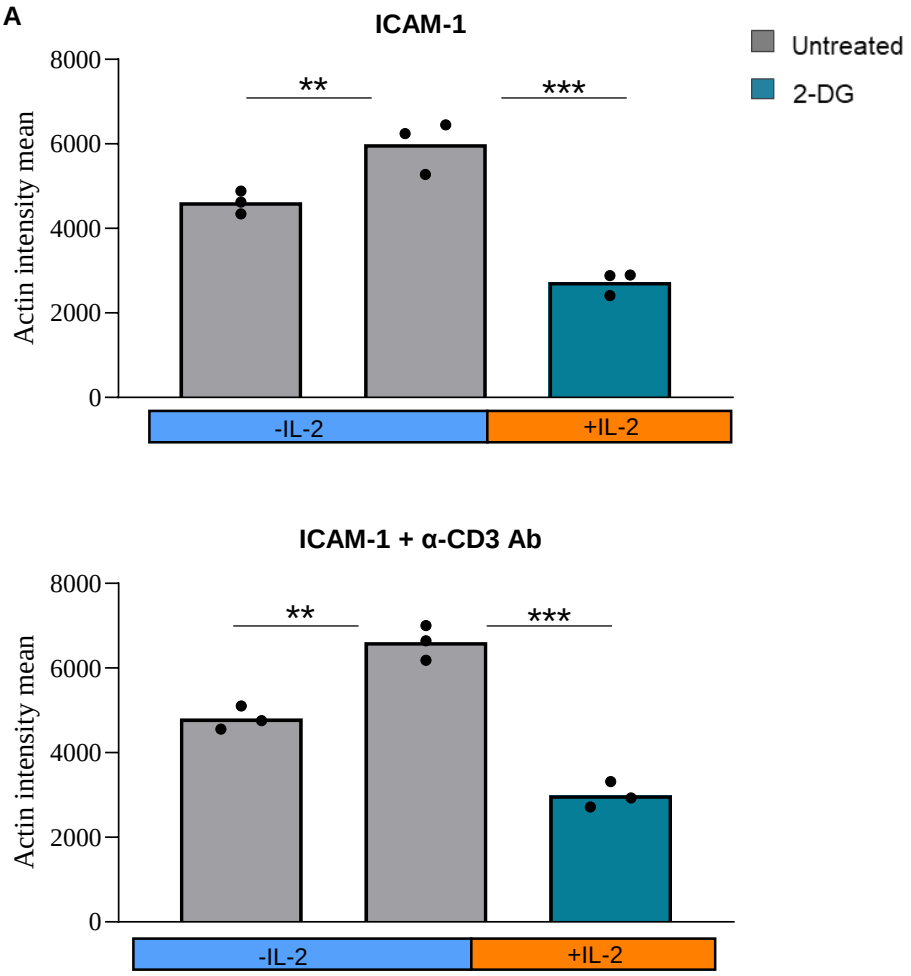

Figure S6. Change in F-actin intensity following treatment with IL2 and 2DG.

(A) Mean actin intensity of cells from three healthy donors stimulated with ICAM-1 or ICAM-1/anti-CD3 Ab and treated with IL-2 and 2-DG, as indicated.One-way Anova comparison test was used for statistical evaluation. ** = $p \leq 0.01$; *** = $p \leq 0.001$.

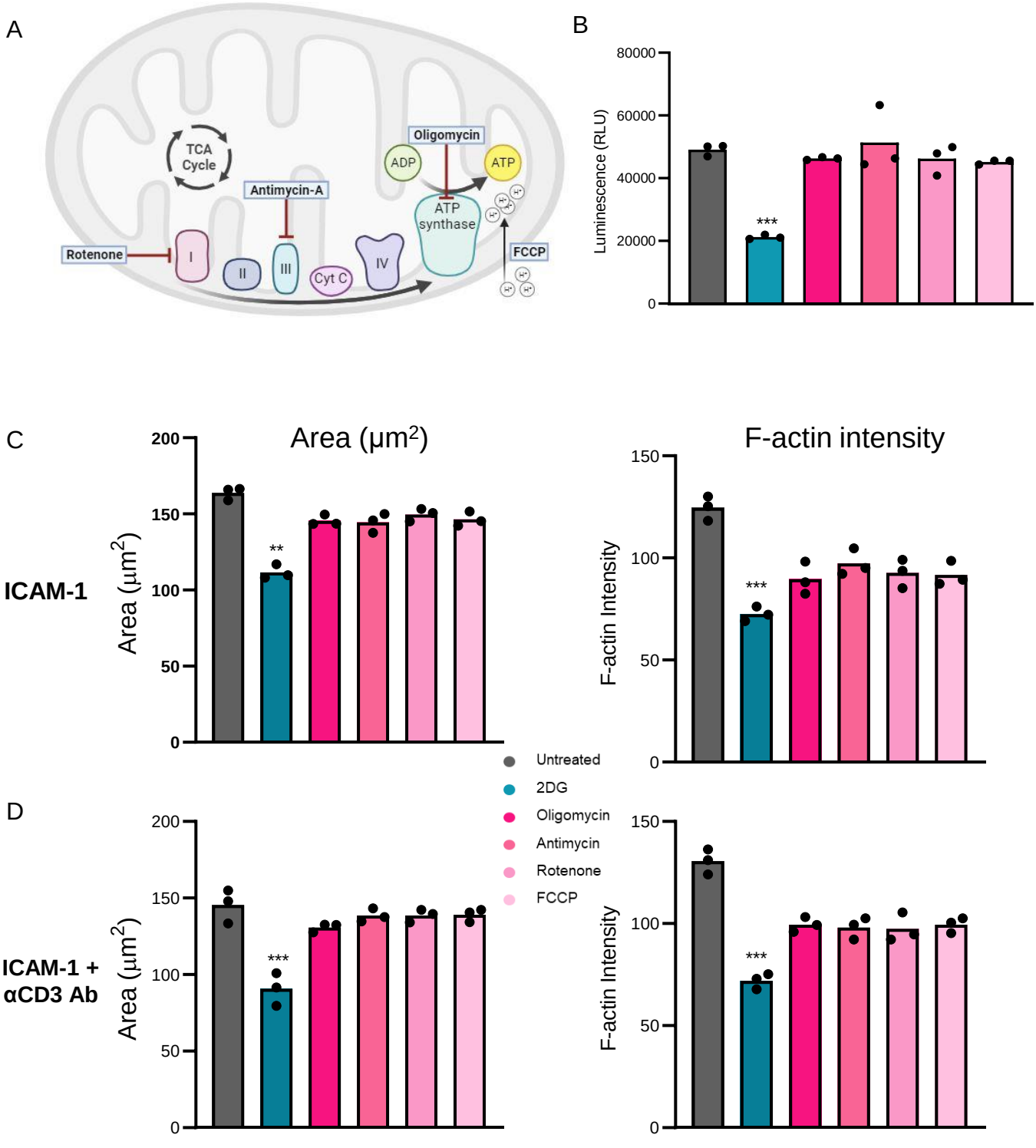

Figure S7. Effect of 2DG and OXPHOS inhibitors on T-cell area and F-actin intensity.

(A) Schematic representing the effect of each drug on the OXPHOS pathway.
(B) ATP content as measured by the CellTiterGlo luminescence assay. Mean of triplicate measurements for 3 donors are shown
(C) Mean F-actin intensity and cell area values extracted from $CD8^+$ T cells from three healthy donors treated with 2DG, Oligomycin, Antimycin, Rotenone or FCCP, seeded on ICAM-1 surfaces.
(D) Mean F-actin intensity and cell area values extracted from $CD8^+$ T cells from three healthy donors treated with 2DG, Oligomycin, Antimycin, Rotenone or FCCP, seeded on ICAM-1 + αCD3 Ab surfaces.

Paired T-test was used for statistical evaluation of all the panels. ns = $p > 0.05$; * = $p \leq 0.05$; ** = $p \leq 0.01$; *** * = $p \leq 0.001$; **** * = $p \leq 0.0001$.

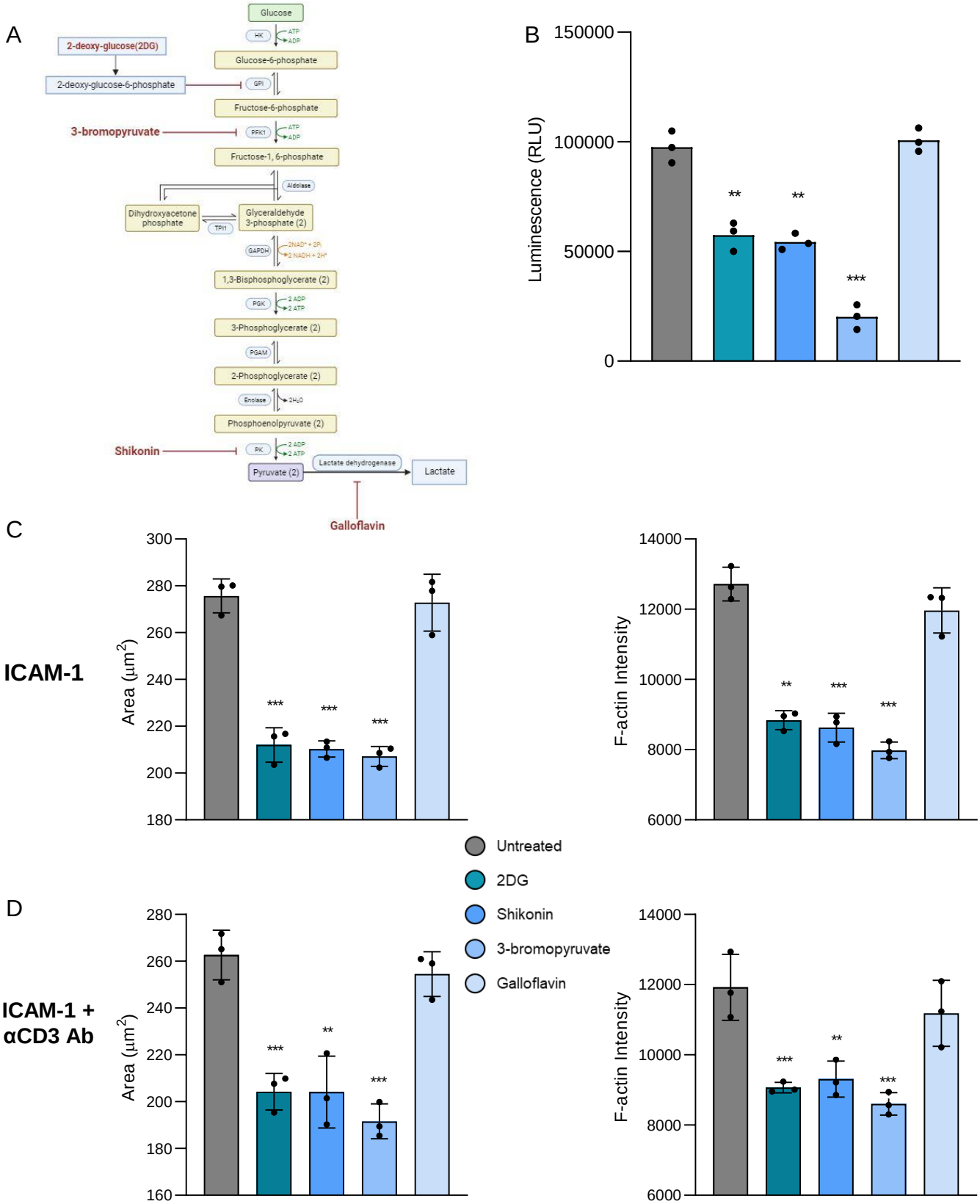

Figure S8. Effect of glycolytic inhibitors on T-cell area and F-actin intensity.

(A) Schematic representing the effect of each glycolytic inhibitor on the glycolysis pathway.
(B) ATP content as measured by the CellTiterGlo luminescence assay. Mean of triplicate measurements for 3 donors are shown
(C) Mean F-actin intensity and cell area values extracted from $CD8^+$ T cells from three healthy donors treated with 2DG, Shikonin, 3-bromopyruvate and Galloflavin, seeded on ICAM-1 surfaces.
(D) Mean F-actin intensity and cell area values extracted from $CD8^+$ T cells from three healthy donors treated with 2DG, Shikonin, 3-bromopyruvate and Galloflavin, seeded on ICAM-1 + αCD3 Ab surfaces.

Paired T-test was used for statistical evaluation of all the panels. ns = $p > 0.05$; * = $p \leq 0.05$; ** = $p \leq 0.01$; *** * = $p \leq 0.001$; **** * = $p \leq 0.0001$.

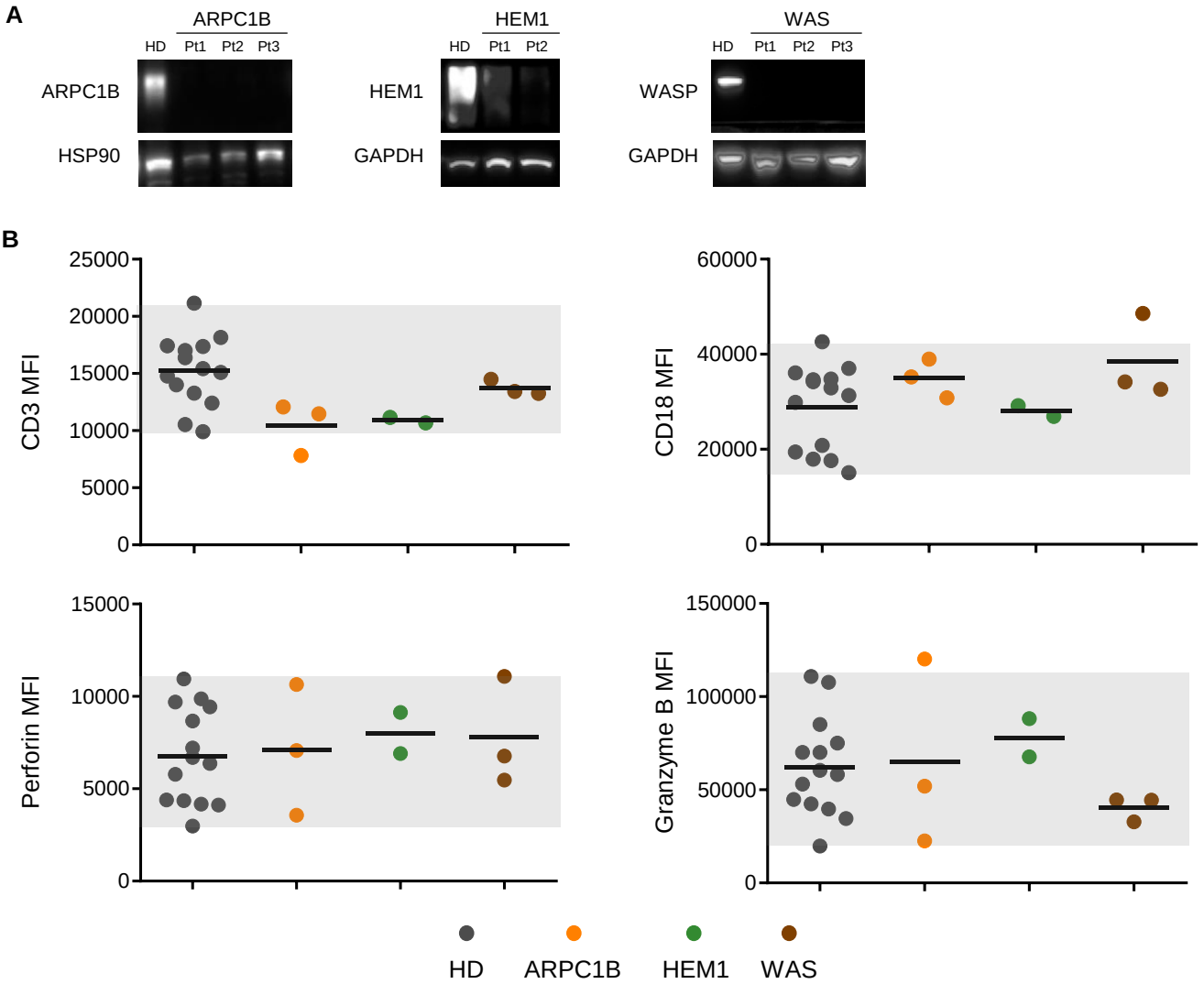

C

Gene (Protein)	Patient ID	Sex	Mutation
ARPC1B	Pt-1	M	c.622G>T
	Pt-2	M	7:98988627 G>GGT
	Pt-3	M	n.c.G623del-TC
WAS (WASP)	Pt-1	M	c.A1509C
	Pt-2	M	484-485 del AG
	Pt-3	M	c.G1453A
HEM1 (NCKAP1L)	Pt-1	F	12:54902194 c.C385T
	Pt-2	F	

Figure S9. Phenotypic characterisation of the CD8⁺ T cell library

(A) Western-blot analysis of the expression of actin-related proteins in T cells from the indicated patients and healthy donors. HSP90 or GAPDH were revealed in parallel.

(B) Measurement of surface CD3 and CD18 and intracellular Perforin and Granzyme B in healthy donor and patient CD8⁺ T cells. The grey squares indicate the normal expression range as determined by the distribution of values across the 14 healthy donor samples.

(C) Table presenting the mutational status of the patients with actin-related inborn errors of immunity.